# PROBING PARTICLE PRODUCTION IN Au+Au COLLISIONS AT $\sqrt{s_{NN}} = 200$ GeV USING SPECTATORS

*A thesis Submitted*
in Partial Fulfilment of the Requirements
for the Degree of

**MASTER OF SCIENCE**

***by***

**Somadutta Bhatta**

***to the***

**School of Physical Sciences**

**National Institute of Science Education and Research**

**Bhubaneswar**

**Date: 10.05.2018**

# DEDICATION

I dedicate this work to my loving parents and teachers.

## DECLARATION

I hereby declare that I am the sole author of this thesis in partial fulfillment of the requirements for a postgraduate degree from National Institute of Science Education and Research (NISER). I authorize NISER to lend this thesis to other institutions or individuals for the purpose of scholarly research.

Signature of the Student
Date:

The thesis work reported in the thesis entitled "Probing particle production in Au+Au collisions at $\sqrt{s_{NN}}$ = 200 GeV using spectators" was carried out under my supervision, in the school of physical sciences at NISER, Bhubaneswar, India.

Signature of the thesis supervisor
School:
Date:

## ACKNOWLEDGEMENTS

First and foremost, I wish to thank my supervisor Prof. Bedangadas Mohanty for introducing me to the exciting field of Experimental High Energy Physics and supervising this work. Without his encouragement, support and advice this work would not have been possible. I would also like to take this chance to express my gratitude to all the Experimental High Energy Physics lab members at NISER, especially Vipul Bairathi and Md. Nasim for their help, guidance, and discussions during the course of this work. Next, a big thanks to all my friends who continue to believe in me and have kept my spirit high during difficult times. I also acknowledge the support and love my parents have shown during the period of my M.Sc at NISER and have continually pushed me to achieve my full potential.

Finally, I would like to thank my luck for allowing me to interact with and learn from some of the best teachers, here at NISER. Their continuous support, care, guidance and most importantly their passion for science will always continue to inspire me.

# ABSTRACT

Events in heavy ion collisions are categorized into centralities, usually based on charged particle multiplicity. But, there are event-by-event fluctuations in the initial event conditions for a given centrality. The access to these variations are limited and it is very difficult to select particular events with definite initial configuration. The categorization of events into centralities allows us to obtain centrality averaged values only.

A study done recently [1] demonstrated that by performing a further binning over spectator neutrons count in addition to the standard centrality binning based on charged particle multiplicity, it is possible to probe the fireball with different initial state conditions. This study was done for Pb+Pb collision at $\sqrt{s_{NN}}$= 2.76 TeV using a multiphase transport model (AMPT). This thesis explores a similar approach in probing initial state using the actual experimental data from Au+Au collision at $\sqrt{s_{NN}}$= 200 GeV through the spectator neutron number (measured by the Zero Degree Calorimeter (ZDC)) in the STAR detector.

We find that in the data collected from STAR detector for Au+Au collisions at 200 GeV, this novel method of binning gives us a better handle at selecting events with specific initial conditions. The initial states that can be accessed by this new procedure cannot be accessed even by finer centrality definition (by multiplicity). This new procedure of choosing initial conditions strongly breaks some previously postulated scaling relations between $v_2/\epsilon_2$ vs $\frac{1}{s}\frac{dN_{ch}}{d\eta}$ and acoustic scaling relation for centrality (by multiplicity) averaged values. The proposed study in this thesis allows for access to new initial conditions in heavy-ion collisions that can be studied in detail in future.

# Contents

# List of Figures

# List of Tables

# Chapter 1

# Introduction

In Heavy Ion Collisions (HIC), we have several experimental observables. Some are "Event variables" like azimuthal anisotropy of produced particles, multiplicity and some are "Track variables" like momentum etc. But, the information on the initial state of the collisions is highly limited. Although the energies of the colliding nuclei are fixed, their geometrical orientation with respect to each other (eg: impact parameter (b)) and nucleon positions inside them cannot be determined on an event to event basis. These variables are very important for studying the event structure in greater details.

In HIC, the events are categorized based only on their centralities (based on multiplicity). This is indicative of the impact parameter of the events (Fig. 1.1). Measurement of experimental variables within each centrality provides their centrality averaged values. But, characteristics of events within each centrality believed to be of similar initial conditions, vary from each other. The access to these variations are limited. In order to study these variations in each centrality in details, we look for other initial state observables. The total number of "Spectator Neutrons" for each event is the observable which is considered in this analysis. We have tried to implement categorization of events on the basis of Left going spectator neutrons+Right going spectator neutrons (L+R) on top of the standard categorization on basis of centralities based on charged particle multiplicity. Using this new procedure, we check how these new bins add-up to show the cumulative property of the whole centrality bins and if this new categorization of events challenges some previously established

physics conclusions.

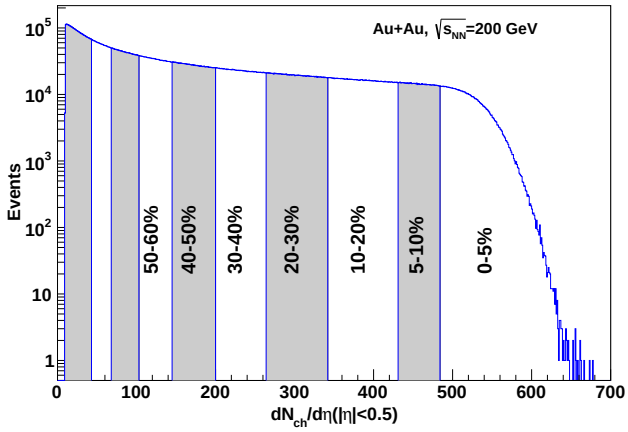


Figure 1.1: Division of charged particle multiplicity distribution at mid-rapidity (RefMult) into 0-5%, 5-10%, ....70-80% and 80-100% centralities. This RefMult data is obtained from the STAR experiment.

# Chapter 2

# Standard Model

The standard model is a theoretical model which attempts to explain different fundamental constituent particles of matter around us and the forces that govern the interaction between them. Both experimental and theoretical branches of high energy physics have contributed towards it's formulation. The standard model has been successful in explaining electromagnetic, weak and strong interactions and forms the foundation of our understanding of the forces and fundamental particles of nature. It has not unified gravitational force with other three forces yet and is unable to explain many observations and postulations like non-zero neutrino mass, the presence of dark matter, hierarchy problem etc.

Elementary particles in the standard model are divided into 3 generations. These three generations differ only in their masses from each other. Each generation is divided into two quarks and two leptons. So in total, there are 6 types of quarks called flavours: up (u) and down (d), charm (c) and strange (s), top (t) and bottom (b). The top quark is the heaviest (mass$\sim$177 GeV) and therefore was discovered long after the discovery of the bottom quark (which is of much smaller mass $\sim$4.18 GeV), when accelerators with high enough energy became available. The leptons are the electron (e), muon ($\mu$), tau ($\tau$) and their corresponding neutrinos ($\nu_e$, $\nu_\mu$, $\nu_\tau$). There are four fundamental forces: the electromagnetic force, mediated by the photon ($\gamma$), the weak force, mediated by the W and Z gauge bosons ($W^+$, $W^-$, $Z^0$), the strong force, mediated by the gluons (g) and gravitational force, mediated by the not yet discovered Gravitons. The photon and the gluons are massless, while the W and Z

bosons are massive. The force mediators ($\gamma$, $W^+$, $W^-$, $Z^0$, g) have spin 1. The Graviton is proposed to have spin 2. All the elementary particles can interact via the weak force, those who are electrically charged interact additionally via the electromagnetic force and the quarks can also have interactions via the strong force.

The standard model includes a formalism to describe the electromagnetic and weak forces with Electro-Weak theory and it describes the strong force with quantum chromodynamics (QCD). Gravity and electromagnetism are long-range forces while the weak and strong interactions are short-ranged. The weak interaction is seen in radioactive decays and the strong interaction binds the quarks together in hadrons and the nucleons inside the nucleus of an atom.

The strength of a force is characterised by its coupling, $\alpha$. This coupling depends on the energy involved in the interaction. At energies which can be observed in daily life, the coupling of all forces is very different. If the coupling $\alpha_s$ for the strong interactions is taken to be of order 1, then for the electromagnetic interactions $\alpha_{em} = 10^{-3}$ , for the weak interactions $\alpha_w = 10^{-16}$ and for gravity it is lowest ($\alpha_g = 10^{-41}$).

However, as the energy goes up, the coupling constants approach each other and may at some high energy be equal. This might make it possible to describe all forces in a single formalism: a Grand Unified Theory. But this can happen only at energies around $10^{19}$ GeV [2].

## QCD

The strong force binds quarks together by the exchange of gluons. The gluons being coloured can also interact with each other (just like two charged particles can interact by electromagnetic interaction). The charge, in this case, is called colour charge and it comes in 3 varieties: red (r), green (g) and blue (b). Quarks have a colour charge and anti-quarks have anti-colour (anti-red ($\bar{r}$), anti-green ($\bar{g}$) and anti-blue ($\bar{b}$)) charge. The gluons have a colour and an anti-colour charge (Fig. 2.1) [3].

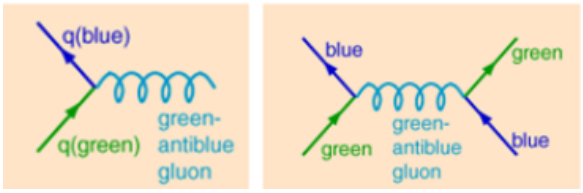


Figure 2.1: Feynman diagrams of interaction between quarks and gluons.

So, there can be the following gluons:

$$(r\bar{b} + b\bar{r})/\sqrt{2}$$

$$(r\bar{g} + g\bar{r})/\sqrt{2}$$

$$(g\bar{b} + b\bar{g})/\sqrt{2}$$

$$(r\bar{r} - b\bar{b})/\sqrt{2}$$

$$-i(r\bar{b} - b\bar{r})/\sqrt{2}$$

$$-i(r\bar{g} - g\bar{r})/\sqrt{2}$$

$$-i(b\bar{g} - g\bar{b})/\sqrt{2}$$

$$(r\bar{r} + b\bar{b} - 2g\bar{g})/\sqrt{6}$$

This can also be explained by existence of only and exactly 8 independent SU(3) (hermitian matrices with 0 trace) matrices (each of which represents a gluon). The

above combinations can be obtained from the following 8 matrices if we consider the three horizontal lines to be consisting of r, b, g and the three columns as $\bar{r}$, $\bar{b}$ and $\bar{g}$.

$$\begin{bmatrix} 1 & 0 & 0 \\ 0 & -1 & 0 \\ 0 & 0 & 0 \end{bmatrix} \begin{bmatrix} 0 & 0 & 0 \\ 0 & 1 & 0 \\ 0 & 0 & -1 \end{bmatrix}, \begin{bmatrix} 1 & 0 & 0 \\ 0 & 0 & 0 \\ 0 & 0 & -1 \end{bmatrix}, \begin{bmatrix} 0 & -i & 0 \\ i & 0 & 0 \\ 0 & 0 & 0 \end{bmatrix},$$

$$\begin{bmatrix} 0 & 0 & i \\ 0 & 0 & 0 \\ -i & 0 & 0 \end{bmatrix} \begin{bmatrix} 0 & 0 & 0 \\ 0 & 0 & i \\ 0 & -i & 0 \end{bmatrix} \begin{bmatrix} 0 & -1 & 0 \\ 1 & 0 & 0 \\ 0 & 0 & 0 \end{bmatrix} \begin{bmatrix} 0 & 0 & 1 \\ 0 & 0 & 0 \\ -1 & 0 & 0 \end{bmatrix} \begin{bmatrix} 0 & 0 & 0 \\ 0 & 0 & 1 \\ 0 & -1 & 0 \end{bmatrix}$$

But from the first three matrices, only two are linearly independent. Therefore, there are exactly 8 types of gluons, not 9[3].

The coupling constant of strong interaction is given as [4]:

$$\alpha_s = \frac{12\pi}{(11n - 2f)ln(|Q^2|/\Lambda^2)}$$

Where '$Q^2$' is the amount of momentum transfer, 'n' is the number of colours and 'f' is the number of flavours and '$\Lambda$' is the scale parameter. $\Lambda$ is experimentally determined to be $\sim$217 MeV [5].

The potential due to the strong force between two quarks increases as they are separated, while the potential due to the electromagnetic force between two charged particles diminishes with distance. With increasing distance the potential energy between the two quarks increases without limit. It would therefore, take an infinite amount of energy to separate them completely. This is why they are never seen as a single particle but are always confined in a colour neutral hadron. This is called ***confinement***. However, when two quarks are close to one another, as they are inside a hadron, they interact only weakly. Within this small volume they almost resemble free particles. This is known as ***asymptotic freedom***. Under high momentum/energy transfer (i.e low $\alpha$), the quarks show asymptotic freedom (the logarithmic decay of the coupling with increase in energy transferred) (Fig. 2.2), and for the low momentum transfer

they show confinement [6].

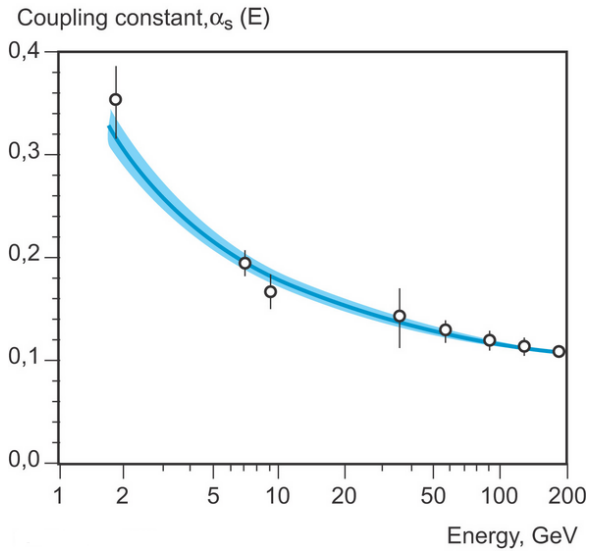


Figure 2.2: The experimentally measured values of the effective gauge coupling $\alpha_s(q)$ confirm the theoretically expected behaviour at high energies (compilation of the Particle Data Group) [7].

Calculations from Lattice QCD (at high $\alpha_s$ i.e in low energy transfer regime) predict that a phase transition can occur from hadronic matter to a system of deconfined quarks and gluons (Fig. 2.3) as the deconfinement leads to availability of higher numbers of degrees of freedom.

When the nuclei collide at ultra-relativistic energy, it results in high temperature or density or both. This state is thought to consist of asymptotically free quarks and gluons, which are the basic building blocks of matter. This state of matter is called Quark Gluon Plasma (QGP).

Ions of heavy elements, such as lead or gold, consist of many nucleons. Collision between two heavy ions can be viewed as a superposition of many independent nucleon-nucleon collisions (although the scenario is not that simple and the collisions that the nucleons can experience are not independent). A nucleon of one nucleus can collide

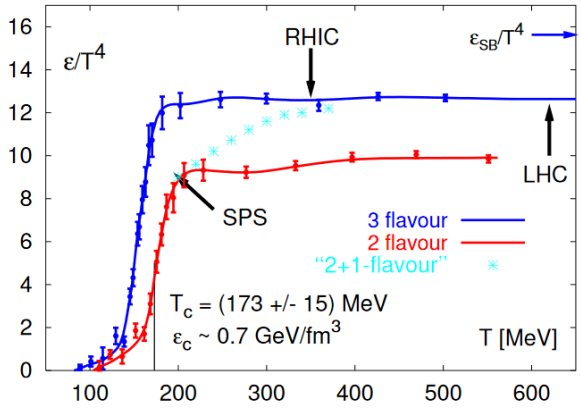


Figure 2.3: The lattice calculations for transitions from hadronic to QGP phase. These calcuations were carried out using 2 and 3 light quarks and 2 light quark plus 1 heavy quark. Phase transition occurs at a temperature of around 173 MeV and energy density $\sim$0.7 GeV/fm$^3$. The blue arrow at right-hand top of the figure denotes the Stefan-Boltzmann limit for non-interacting massless quark gas. This indicates that the quark-gluon plasma is a weakly interacting fluid [8].

with many nucleons of the other nucleus and in this way it deposits a large part of it's energy in the collision region. This energy is available for the production of particles.

## Quark Gluon Plasma

The energy density in the collision region can become very high due to the deposited energy. If it is high enough ($\sim 0.7$ GeV/fm$^3$), QGP can be formed, which will exist only for a short time because the system cools as it expands after the collision. When the system gets below the critical temperature it enters a mixed phase (if the transition is first order) or a cross-over until all quarks are again bound inside hadrons.

As the energy in the system decreases, at $T_c$ (Critical temperature) the hadrons start to form. Upon further cooling, at $T_{ch}$ (chemical freezeout temperature) the inelastic interactions between hadrons stop and relative abundances remain fixed. After this the elastic collisons goes on till $T_{kin}$ (Kinetic freezeout temperature) and then kinetic freezeout happens (Fig. 2.4). At $T_{kin}$, the momentum distribution of particles gets fixed. After this, the produced particles stream freely to reach the detectors.

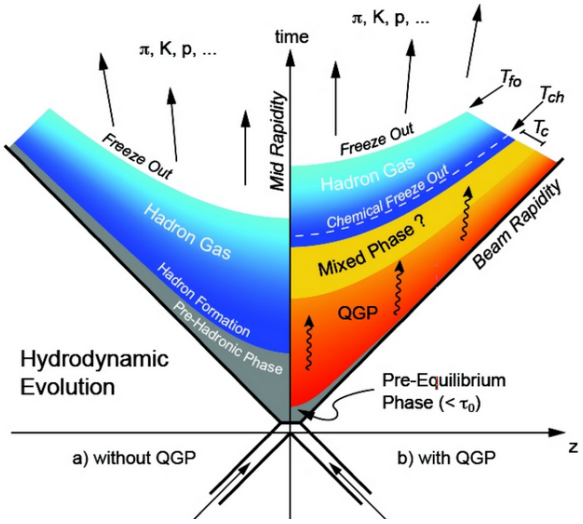


Figure 2.4: Space-time evolution after the heavy ion collision. The scenario on left represents the case where no QGP is formed ($T < T_c$) and on right is the case with QGP formation ($T > T_c$) [6].

## Signatures of QGP

As QGP cannot be observed directly, we check for different indirect observations to see whether QGP is formed. These signatures of QGP are as follows:

1) **Jet Quenching**:

Partons with high momentum generate high momentum hadrons. However, when these partons traverse the dense QGP system they lose energy resulting in a reduced yield of high momentum hadrons [6].

The effects of parton energy loss can be seen in the azimuthal distribution of back-to-back jets that are formed. If the parton loses energy by traversing the QGP before hadronisation, the resulting jet will have a lower total energy, i.e the jet is quenched. It can also be totally stopped inside the system. In events where jets are produced back-to-back, at the edge of the collision volume, the path through the system of one of the partons leading to a jet is much longer than for the other. This jet is quenched or totally suppressed while the other suffers almost no quenching (Fig. 2.5). Such quenching is not present in proton-proton collisions and thus points to the formation of a dense system.

2) **Strangeness Enhancement**:

In a proton-proton collision, strange quark pairs ($s\bar{s}$) can be formed from the available kinetic energy. Strange quarks are not present in the protons before the collision. The probability to form a strange quark pair is small and therefore the number of strange particles, produced in the collision is also small [3]. In a medium with QGP, the increased probability of $g\bar{g}$ combination gives rise to an increased strange quark yield.

3) **J/$\psi$ Suppression**:

The J/$\psi$ particle is a bound state of $c$ and $\bar{c}$. J/$\psi$ yield would be suppressed in a

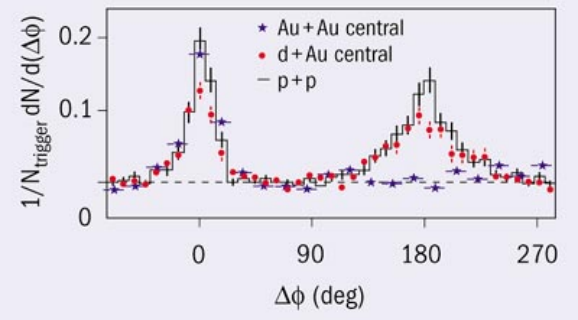


Figure 2.5: Data from the STAR experiment show angular correlations between pairs of high transverse-momentum charged particles, referenced to a "trigger" particle that is required to have $p_T$ greater than 4 GeV. The proton-proton and deuteron-gold collision data indicate back-to-back pairs of jets (a peak associated with the trigger particle at $\Delta\phi = 0$ degrees and a somewhat broadened recoil peak at 180 degrees). The central gold-gold data indicate the characteristic jet peak around the trigger particle, at 0 degrees, but the recoil jet is absent [9].

deconfined medium due to the Debye screening of the attractive colour force which binds the c and $\bar{c}$ quarks together. J/$\psi$ suppression is an interesting signature of QGP formation because it probes the state of matter in the earliest stages of the collision, since $c\bar{c}$ pairs can only be produced at that time (from hard scatterings).

4) **Collective Flow**:

If in a heavy ion collision a system is formed in which particles undergo multiple interactions, leading to local thermal equilibrium and a common velocity distribution, that system will show collective effects in its subsequent evolution. The evolution of the system can then be described by hydrodynamics. This collective flow, is sensitive to the strength of the interactions between particles and the hydrodynamical equation of state of the system. At low centre of mass energies, collective flow mostly reflects the properties of hadronic matter whereas at higher centre of mass energies the contribution from a partonic phase (possibly the QGP) becomes more and more dominant.

The system formed in a heavy ion collision is surrounded by vacuum. This gives rise to a pressure gradient from the dense centre to the boundary of the system. In central heavy ion collisions this pressure gradient is radially symmetric and gives a boost to all particles that are formed in the system, pushing them radially outward. This means that on top of their thermal motion (governed by classical Maxwell-Boltzmann statistics), the particles get a radial velocity component.

The radial velocity component results in an increase of the momentum (p = mv) which is proportional to the mass of the particle. Therefore, the effect of radial flow is most pronounced for heavy particles. The transverse momentum spectra of hadrons, in particular heavy particles, are influenced by radial flow, flattening them at low transverse momentum ($p_T$). For peripheral collisions, the interaction region is elliptically shaped (Fig. 2.6). Thus, the pressure gradient along the smaller axis is higher than the pressure gradient along the longer axis of this elliptical region. This pressure difference along the two axis pushes the particles outwards more along the shorter axis than along the longer axis. Thus, the initial spatial anisotropy leads to a final momentum space anisotropy. This azimuthal angle anisotropy in number of particles is called elliptic flow.

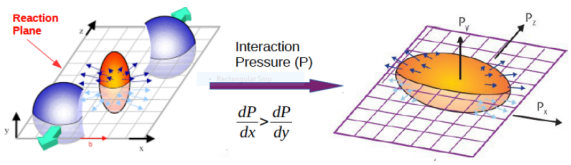


Figure 2.6: Non-central collisions leads to spatial anisotropy which leads to anisotropy in momentum space.

For non-central heavy ion collisions the shape of the interaction region depends on the impact parameter 'b' of the collision. The impact parameter is defined by the distance between the centres of the two colliding nuclei. Together with the z-axis (beam direction) it defines the reaction plane, of which the azimuthal angle is $\psi_R$. In

the middle, the reaction volume is elliptically shaped, while the spectators (particles outside the overlap between the two nuclei) continue in the beam direction z.

In a collision between two protons, particles are produced isotropically in the transverse plane. This means that in a heavy ion collision, where many protons collide, particle production is isotropic as well if all these proton-proton collisions are independent of each other. If on the other hand, in the collision system particles undergo multiple interactions the azimuthal transverse momentum distribution is modified due to the anisotropy of the reaction volume (Fig. 2.7).
This can be characterised by the Fourier expansion of the momentum distribution with respect to the reaction plane angle $\psi_R$,
The n$^{th}$ flow coefficient is given by:

$$v_n = \langle\langle cos(n(\phi - \psi_R))\rangle_p\rangle_{evt.}$$

The brackets denote an average over all particles 'p' in the event and all events. Note that $v_n$, being the average of a cosine, is always smaller than 1. At zero impact parameter the reaction volume is spherical resulting in a uniform azimuthal distribution of particles, while at a finite impact parameter the reaction volume is anisotropic and the coefficients $v_n$ will be nonzero. Each Fourier coefficient (harmonic) reflects a different type of anisotropy (Fig. 2.7).

The first harmonic $v_1$ represents an overall shift of the distribution in the transverse plane and is called directed flow. The second harmonic $v_2$ represents an elliptical volume and is called elliptic flow. The third harmonic (triangular flow) gives a triangular modulation and the fourth a squared modulation. For matter at midrapidity (around $\eta = \frac{1}{2} ln \frac{P+P_z}{P-P_z} = -ln[tan(\frac{\theta}{2})]$=0) the second harmonic, elliptic flow, is dominant.

The data from RHIC (Relativistic Heavy Ion Collision) experiment for $v_2$ vs trans-

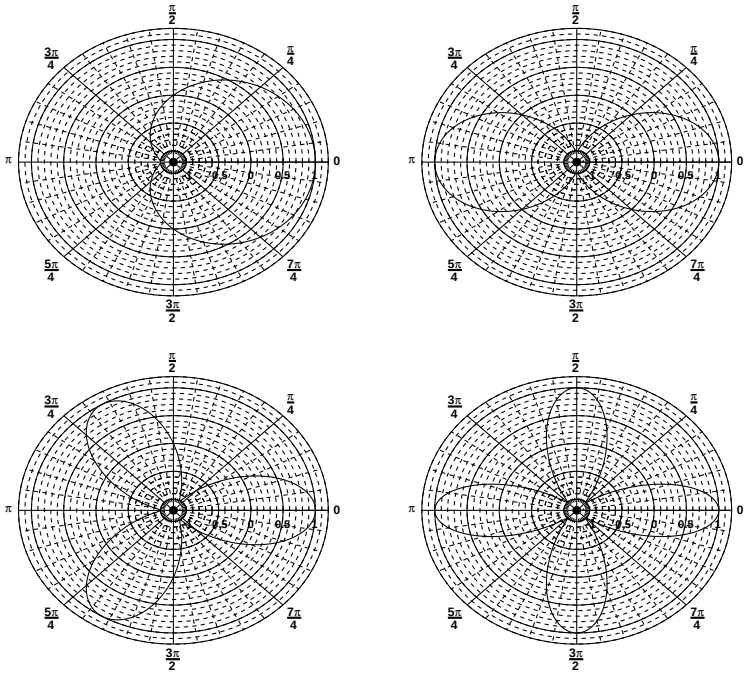

Figure 2.7: The first four flow harmonics in the transverse plane in polar coordinates (top left: n=1, top right: n=2, bottom left: n=3, bottom right: n=4).

verse momentum ($p_T$) is shown in Fig. 2.8:

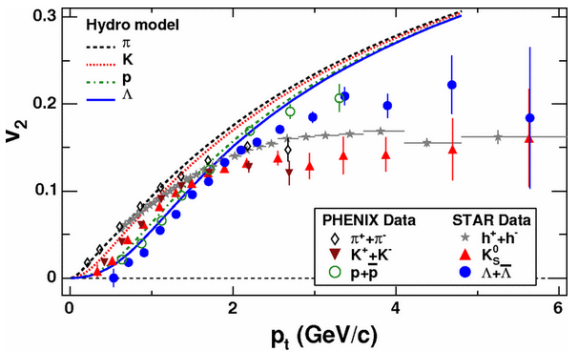


Figure 2.8: Measurements of $v_2(p_T)$ for identified particles in Au+Au collisions for 0-80% centrality at RHIC. The lines are the results from hydrodynamic model calculation [10].

# Chapter 3

# STAR Detector

The STAR detector was built to study behaviour of strongly interacting matter at high energy density and to search for the signatures of QGP. To achieve this, nuclei are collided with each other at high energies resulting in formation of a large number of particles from partonic interactions. The temperature in the region of nuclei-nuclei collision becomes so high that it mimics the temperature at the early stage of universe. This magnificent detector (Fig. 3.1) is as seen below:

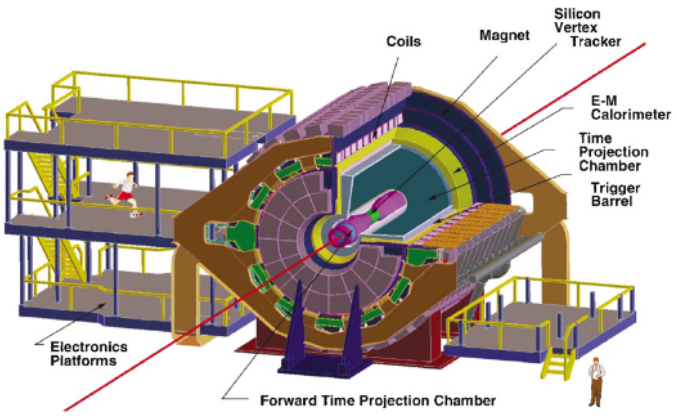


Figure 3.1: The cross-section view of the STAR detector.

A room temperature solenoidal magnet with a uniform magnetic field of maximum value 0.5 T provides for charged particle momentum analysis. Charged particle tracking close to the interaction region is accomplished by a Silicon Vertex Tracker (SVT) consisting of 216 silicon drift detectors arranged in three cylindrical layers at distances of approximately 7, 11 and 15 cm from the beam axis. The silicon detectors cover a pseudo-rapidity $|\eta|$ <1 with complete azimuthal coverage. Silicon tracking close to the interaction allows precision localization of the primary interaction ver-

tex and identification of secondary vertices from weak decays. A large volume Time Projection Chamber (TPC) for charged particle tracking and particle identification is located at a radial distance from 50 to 200 cm from the beam axis. The TPC is 4 m long and it covers a pseudo-rapidity range of $|\eta| < 1.8$ for tracking with complete azimuthal symmetry. The electromagnetic calorimeter helps in measurement of the transverse energy of events and measures high transverse momentum photons, electrons, and electromagnetically decaying hadrons. This has a coverage of $|\eta| < 1$. The Zero-Degree Calorimeters (ZDC) are installed on both ends of the detector at an angle of $\sim$0.8 mRad and helps in detection of incoming spectator neutrons and protons [11]. But protons being charged particles, bend in the magnetic field and hit the walls before being incident on the detector. The beam pipe radius is 4 cm.

# Chapter 4

# Measurement of Elliptic Flow Coefficients

Particles produced in an heavy-ion collision are detected by the detector and thus we get information on their azimuthal distribution. For non-central collisions, the evolution of the system formed after collision is dependent upon its initial spatial anisotropy. Due to the interaction of the particles in the reaction volume, the medium thermalises. This allows us to describe the system in terms of thermodynamic quantities. The region has high temperature and pressure. The anisotropy of the reaction volume and the existing vaccum outside this volume causes a pressure gradient inside this reaction volume. For the elliptical overlap region (peripheral collisions), as minor axis is smaller than the major axis, a pressure gradient develops. This leads to a subsequent momentum space anisotropy. Thus, the initial spatial anisotropy gives rise to final momentum space anisotropy. We measure this anisotropy with reference to a particular plane, namely "Reaction Plane". This plane is defined for each event by the impact parameter (vector from the center of one of the colliding nuclei to the center of the other nucleus) and the beam axis (z-axis).

Following is a derivation of the flow coefficients [12]:

Because the physical quantity of interest here is azimuthal distribution of the produced particles, i.e $r(\phi)$ and it has periodicity of $2\pi$, we expand it with a Fourier series.

$$r(\phi) = \frac{x_0}{2\pi} + \frac{1}{\pi}\sum_{n=1}^{\infty}[x_n.cos(n\phi) + y_n.sin(n\phi)]$$

where, $x_n = \int_0^{2\pi} r(\phi)cos(n\phi)d\phi$ and $y_n = \int_0^{2\pi} r(\phi)sin(n\phi)d\phi$.

For a given pair of ($x_n$, $y_n$), the flow vector is defined as

$$v_n = \sqrt{x_n^2 + y_n^2}$$

We can write,

$$\begin{aligned}\langle cos(n\phi)\rangle &= \frac{\int_0^{2\pi} r(\phi)cos(n\phi)d\phi}{\int_o^{2\pi} r(\phi)d\phi} \\ &= \frac{\frac{1}{\pi}v_n \int_0^{2\pi} cos^2(n\phi)d\phi}{\int_0^{2\pi} r(\phi)d\phi} \\ &= \frac{v_n}{v_0}\end{aligned}$$

where we used $\int_0^{2\pi} cos(mx)cos(nx)dx = \pi\delta_{mn}$.

We can use a normalised distribution $r(\phi)$, for which $v_0 = \int_0^{2\pi} r(\phi)d\phi = 1$. Thus obtaining $v_n = \langle cos(n\phi)\rangle$. For n=1, we get directed flow, for n=2 we get elliptic flow and for n=3 we get triangular flow coefficients and so on. When flow harmonics are considered as a function of transverse momentum and rapidity $v_n(p_T, y)$, we refer to them as differential flow.

Hence, the elliptic flow coefficient is defined as

$$v_2 = \langle\langle cos[2(\phi - \Psi_R)]\rangle\rangle$$

where $\Psi_R$ is the reaction plane angle, i.e the angle formed by the impact parameter vector and x-axis. The double average is over all the particles in an event and over all the events

So, it is crucial to calculate $\Psi_R$ for each event to calculate $v_2$. As the impact parameter vector cannot be measured in the experiment, the reaction plane angle required for the $v_2$ calculation cannot be obtained. So, we use a proxy for reaction plane, namely "Event plane". The event plane angle is calculated as follows;

We define flow vectors $Q_n$ such that

$$x_n = Q_n.cos(n\psi_n) = \sum_{i=1}^{n} w_i.cos(n\phi_i)$$

and

$$y_n = Q_n.sin(n\psi_n) = \sum_{i=1}^{n} w_i.sin(n\phi_i)$$

where $w_i$ is the weight and N is the total number of produced particles in a given event used for flow vector calculation. The weight is most often taken as $p_T$($\phi$, $\eta$ are also taken in several other analysis with different methods of applying those weights). From the values of $x_n$ and $y_n$ we calculate the $n^{th}$ order reaction plane angle $\psi_n$ as

$$\psi_n = \frac{1}{n}tan^{-1}(\frac{\sum_{i=1}^{n} w_i.sin(n\phi_i)}{\sum_{i=1}^{n} w_i.cos(n\phi_i)}) = \frac{1}{n}tan^{-1}\frac{y_n}{x_n}$$

where $\psi_n \epsilon [0, \frac{2\pi}{n}]$.

In this analysis, we have used the Eta-Sub event plane method of event plane calculation in which we divide all the events (between $|\eta| < 1$) in two parts $-1 < \eta < -0.05$ and $0.05 < \eta < 1$. We call the event plane in these ranges $\psi^a$ and $\psi^b$ respectively. We leave a gap of $\Delta\eta$=0.1 so as to remove the autocorrelation between particles in the final calculation of elliptic flow coefficient.

After getting the event plane angle, generally it is not smooth (as impact parameter is random, we expect the event plane distribtion to be uniform). This arises due to detector bias and limited acceptance. To correct/compensate for this dependence, we carry out two types of corrections, "**Recenter Correction**" and "**Shift Correction**".

In Recenter correction, we subtract the mean values of $x_n$ and $y_n$ (averaged over all events) from the respective values of $x_n$ and $y_n$ for each event. These recentered values of $x_n$ and $y_n$ are then used to calculate $\psi_n$. But still then the event plane

doesn't become completely flat. This happens due to presence of higher harmonics from the distribution of event plane angle.

To correct for the presence of the higher harmonics we carry out "Shift Correction". In short, the shift correction fits the unweighted laboratory distribution of the event planes, summed over all events, to a Fourier expansion and devises an event-by-event shifting of the planes needed to make the final distribution isotropic.

The formula for shift correction for one of the eta-ranges is as follows:

$$\psi^{a}_{n,final} = \sum_{i=1}^{m} \frac{2}{n}[-\frac{1}{i}\langle sin(ni\psi)\rangle cos(ni\psi) + \frac{1}{i}\langle cos(ni\psi)\rangle sin(ni\psi)]$$

and likewise for $\psi^{b}_{n,final}$('n' stands for the order of the event plane angle to be shift corrected and m stands for the order of the harmonics upto which the correction is to be applied).

As the number of particles detected in the experiment is limited, there is a limitation on the accuracy upto which the true reaction plane can be found. This introduces a "**Resolution**" factor into the calculation of $v_2$. A resolution of 1 means that the reaction plane is equal to the event plane angle. The resolution factor "R" is given by :

$$R = \sqrt{\langle cos[n(\psi^{a}_{n,final} - \psi^{b}_{n,final})]\rangle}$$

(here n=2 for elliptic flow and n=3 for triangular flow). Because the number of particles are different for different centralities, the resolution value is also different for different centralities.

# Chapter 5

# MC Glauber Model

In heavy ion collision experiments it is impossible to measure the initial conditions/configurations such as impact parameter (b), number of binary nucleon-nucleon collisions ($N_{coll}$), number of participating nucleons ($N_{part}$), eccentricity ($\epsilon$), overlap region area ($\sigma$)etc. So, numerical methods are developed to extract these values from a given system for heavy ion collision by considering the multiple-scattering of nucleons. One such model is the Glauber model.

There are two kinds of Glauber models, namely

1. **Optical Glauber Model**:

In this model, it is assumed that at sufficiently high energies, the nucleons will carry sufficient momentum that they will pass undeflected through each other. Another assumption is that the nucleons move independently in the nucleus and that the size of the nucleus is large compared to the extent of the nucleon-nucleon force. The hypothesis of independent linear trajectories of the constituent nucleons makes it possible to develop simple analytic expressions for the nucleus-nucleus interaction cross section, the number of interacting nucleons and the number of nucleon-nucleon collisions in terms of the basic nucleon-nucleon cross section.

2. **Monte Carlo Glauber Model**:

In the Monte Carlo Glauber model, the two colliding nuclei are assembled in the computer by distributing the nucleons of nucleus A and nucleus B in three dimensional coordinate system according to their respective nuclear density distribution. A random

impact parameter 'b' is then drawn from the distribution $\frac{d\sigma}{db} = 2\pi b$. A nucleus-nucleus collision is treated as a sequence of independent binary nucleon-nucleon collisions and the inelastic nucleon-nucleon cross-section is assumed to be independent of the number of collisions a nucleon underwent before. In the simplest version of the Monte Carlo approach a nucleon-nucleon collision takes place if their distance 'd' in the plane orthogonal to the beam axis satisfies

$$d \leq \frac{\sqrt{\sigma_{NN,inelastic}}}{\pi}$$

where $\sigma_{NN,inelastic}$ is the total inelastic nucleon-nucleon cross-section.

The basic inputs for Glauber Models are as follows:

1. **Nuclear Charge Densities**:

In Glauber models the nuclear density is modelled by three prameter Fermi distribution

$$\rho(r) = \rho_0 . \frac{1 + w(\frac{r}{R})^2}{1 + exp(\frac{r-R}{a})}$$

where $\rho_0$ corresponds to nuclear density at the center of nucleus, 'R' corresponds to nuclear radius, 'a' to the "skin depth" and 'w' characterizes deviations from a spherical shape.

In the Monte Carlo procedure the radius of a nucleon is randomly drawn from the distribution $4\pi r^2 \rho(r)$. The impact parameter of the collision is chosen randomly from a distribution $\frac{dN}{db} \propto b$ up to some large maximum $b_{max} > 2R_A$, where $R_A$ is the radius of partcipating nucleus.

2. **Inelastic Nucleon-Nucleon Cross-Section**:

In the context of high energy nuclear collisions, we are typically interested in multiparticle nucleon-nucleon processes. As the cross section involves processes with low momentum transfer, it is impossible to calculate this using perturbative QCD. Thus,

the measured inelastic nucleon-nucleon cross section $\sigma_{NN,inelastic}$ is used as an input, and provides the only non-trivial beam-energy dependence for Glauber calculations.

By changing the parameters we match the multiplicity distribution obtained from data with the multiplicity distribution obtained from Glauber Model. Once they match (Fig. 5.1), we then used the multiplicity distribution to define centrality classes in data obtained from MC Glauber model simulation. Then, the values for different initial variables for the collisions (eg. eccentricity ($\epsilon$) impact parameter (b), $N_{part}$, system size ($\sigma$) etc.) in different centralities and different L+R bins within each centrality were obtained.

It is important to note the mismatch between multiplicity distribution for glauber model and data for very low and very high multiplicity. At low multplicity, the mismatch arises due to detector inefficiency whereas at high multplicity the mismatch arises due to low statistics.

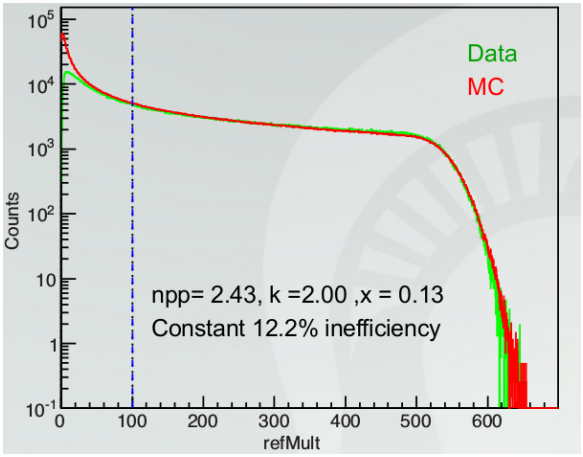


Figure 5.1: Multiplicity distribution from data collected for Au+Au collisions at $\sqrt{s_{NN}}$ = 200 GeV compared with multiplicity distribution obtained from Glauber model for the same system [13]. npp, x, k and efficiency are the different parameters that are varied to match multiplicity distributions obtained from data and Glauber model.

# Chapter 6

# Kinematics

High energy collisions can be characterised by distributions of certain kinetic variables. Some of these kinematic variables are discussed here. The kinematic variables are plotted in this report for Au+Au collisions at $\sqrt{s_{NN}}$ = 200 GeV using ROOT framework [14].

1) **center of mass energy ($\sqrt{s}$)**:

This is the total energy possesssed by the colliding atoms in their center of mass frame.

2) **Impact parameter (b)**:

Imapct parameter is the distance between the centres of two colliding heavy nuclei. Smaller the b, higher is the centrality of the collision

3) **Multiplicity (N)**:

Multiplicity is defined as the total number of particles produced per event.

4) **Phi ($\phi$)**:

This denotes the azimuthal angle of the particle in the transverse plane around the beam axis with the x-axis.

$$\phi = tan^{-1}(\frac{P_y}{P_x})$$

5) **theta ($\theta$)**:

This denotes the angle made by the particle with the z axis (generally taken as the direction of beam) and is defined as

$$\theta = cos^{-1}(\frac{P_z}{p})$$

6) **Rapidity (y)**:

It is defined as

$$y = \frac{1}{2} ln \frac{E + P_z}{E - P_z}$$

This quantity is very useful in high energy experiments as the difference in rapidity of two particles is same in all the frames (invariant) as we prove below:

we have from special theory of relativity;

$$1 - \beta^2 = \frac{1}{\gamma^2}$$

so we can take $\gamma = cosh(\alpha)$ and $\beta\gamma = sinh(\alpha)$; So that

$$tanh(\alpha) = \beta$$

and therefore

$$\alpha = tanh^{-1}(\beta)$$

which is also called the 'Rapidity Parameter' as we just have to calculate this to go from one frame to another.

Lets assume that we have in one frame,

$$y = \frac{1}{2} ln \frac{E + P_z}{E - P_z}$$

and in another frame,

$$y' = \frac{1}{2} ln \frac{E' + p'_z}{E' - p'_z}$$

So,substituting

$$E' = \gamma E - \beta\gamma P_z$$

and

$$P'_z = \gamma P_z - \beta\gamma E$$

We get;

$$y = \frac{1}{2} ln \frac{(1-\beta)(E+P_z)}{(1+\beta)(E-P_z)}$$

$$= \frac{1}{2}[ln\frac{(E+P_z)}{(E-P_z)} - ln\frac{(1+\beta)}{(1-\beta)}] = y - \frac{1}{2} ln\frac{(1+\beta)}{(1-\beta)} = y - \alpha$$

Therefore

$$y' = y - \alpha$$

and

$$y_2 - y_1 = y_2' - y_1'$$

for two events with same $\alpha$.

7) **Pseudo-rapidity ($\eta$)**:

It is defined as

$$\eta = \frac{1}{2} ln \frac{P + P_z}{P - P_z}$$

We have, $cos\theta = \frac{P_z}{P}$. So, $\frac{P+P_z}{P-P_z} = \frac{1+cos\theta}{1-cos\theta} = cot^2\frac{\theta}{2}$.

Therefore,

$$\eta = -ln(tan(\theta/2))$$

Also,

$$-2\eta = 2lntan(\theta/2) \Longrightarrow e^{-2\eta} = tan^2(\theta/2)$$

Using addendo dividendo;

$$\frac{1 - e^{-2\eta}}{1 + e^{-2\eta}} = \frac{1 - tan^2(\theta/2)}{sec^2(\theta/2)}$$

$$\Rightarrow tanh(\eta) = cos(\theta) = \frac{P_z}{P}$$

so,

$$\eta = tanh^{-1}\frac{P_z}{P}$$

In the $\eta$ distribution, we generally observe a dip close to maxima of the $\eta$ distribution,

which can be explained as follows:

We have

$$y = \frac{1}{2} ln[\frac{(\sqrt{m^2 + p_T^2 cosh(\eta)}) + p_T sinh(\eta)}{(\sqrt{m^2 + p_T^2 cosh(\eta)}) - p_T sinh(\eta)}]$$

using $E^2 = P^2 + m^2$, $|P| = p_T cosh(\eta)$ and $P_z = p_T sinh(\eta)$.

$\frac{dN}{d\eta} = \frac{dN}{dy}\frac{dy}{d\eta} = \frac{dN}{dy}\frac{P}{E}$

We have

$$\frac{P}{E} = \frac{\sqrt{E^2 - m^2}}{E}$$

$$= \sqrt{1 - \frac{m^2}{E^2}} = \sqrt{1 - (\frac{m}{\sqrt{p_T^2 + m^2 cosh(y)}})^2}$$

so,

$$\frac{dN}{d\eta} = \frac{dN}{dy}\frac{dy}{d\eta} = \frac{dN}{dy}\sqrt{1 - (\frac{m}{\sqrt{p_T^2 + m^2 coshy}})^2}$$

Also from expression of conversion between y and $\eta$ differentiating y with respect to $\eta$, we get,

$$\frac{dy}{d\eta} = \frac{1}{2}[\frac{(\sqrt{m^2 + p_T^2 cosh(\eta)}) - p_T sinh(\eta)}{(\sqrt{m^2 + p_T^2 cosh\eta}) + p_T sinh(\eta)}]\frac{d}{d\eta}[\frac{(\sqrt{m^2 + p_T^2 cosh(\eta)}) + p_T sinh(\eta)}{(\sqrt{m^2 + p_T^2 cosh(\eta)}) - p_T sinh(\eta)}]$$

$$= \frac{1}{2}.[\frac{1}{(\sqrt{m^2 + p_T^2 cosh(\eta)}) + p_T sinh(\eta)}\frac{d}{d\eta}[(\sqrt{m^2 + p_T^2 cosh(\eta)}) + p_T sinh(\eta)]$$

$$-\frac{1}{(\sqrt{m^2 + p_T^2 cosh(\eta)}) - p_T sinh(\eta)}\frac{d}{d\eta}[(\sqrt{m^2 + p_T^2 cosh(\eta)}) - p_T sinh(\eta)]$$

$$= \frac{1}{2}.[\frac{1}{(\sqrt{m^2 + p_T^2 cosh(\eta)}) + p_T sinh(\eta)} \times (\frac{p_t^2 cosh(\eta) sinh(\eta)}{p_T^2 cosh^2(\eta) + m_0^2} + p_T cosh(\eta))$$

$$-\frac{1}{(\sqrt{m^2 + p_T^2 cosh(\eta)}) - p_T sinh(\eta)} \times (\frac{p_t^2 cosh(\eta) sinh(\eta)}{p_T^2 cosh^2(\eta) + m_0^2} - p_T cosh(\eta))$$

$$= \frac{1}{2}\frac{1}{p_T^2 + m^2}\frac{2(p_T^2 + m^2) p_T cosh(\eta)}{\sqrt{p_T cosh^2(\eta) + m^2}}$$

$$= \frac{p_T cosh(\eta)}{\sqrt{p_T cosh^2(\eta) + m^2}}$$

Therefore,

$$\frac{dN}{d\eta} = \frac{dN}{dy}\sqrt{1 - (\frac{m}{\sqrt{p_T^2 + m^2 cosh(y)}})^2}$$

so, near 0 of $\eta$ axis on $dN/d\eta$ vs $\eta$ distribution, this jacobian term causes a deviation from $dN/dy$ distribution and causes a dip near the maxima of the distribution.

8) **Transverse Momentum ($p_T$)**:

Transverse momentum gives the amount of momentum in the plane transverse (xy plane) to the beam axis (z axis). It is given by:

$$p_T = \sqrt{(P_x^2 + P_y^2)}$$

9) **Transverse Mass ($m_t$)**:

This is given by $\sqrt{E^2 - P_z^2}$ and is lorentz invariant as it is equal to $\sqrt{p_T^2 + m^2}$ which is lorentz invariant.

In high energy collisions $\sqrt{S}$ is the centre of mass energy and is given by:

$$S = (p_1 + p_2)^2 = (E_1 + E_2)^2 - (\vec{P_1}^2 + \vec{P_2}^2)$$

$$= m_1^2 + m_2^2 + 2E_1E_2 - 2\vec{P_1}.\vec{P_2}$$

In centre of mass (CM) frame, $\vec{P_1} + \vec{P_2}$=0.So, $\sqrt{S} = E_1 + E_2$.

If $m_1 = m_2 \Rightarrow E_1 = E_2 = E \Rightarrow \sqrt{S} = 2E$

In CM frame, $|\vec{P_1}| = |\vec{P_2}| = P_{cm}$.

So,$E_1 = \sqrt{P_{cm}^2 + m_1^2}$ and $E_2 = \sqrt{P_{cm}^2 + m_2^2}$

So, substituting in $S = m_1^2 + m_2^2 + 2E_1E_2 - 2\vec{P_1}.\vec{P_2}$ and solving we get,

$$P_{cm} = \frac{1}{2\sqrt{S}}\sqrt{[(S - (m_1 - m_2)^2)(S - (m_1 + m_2)^2)]}$$

If $m_1 = m_2 = m$, $P_{cm} = \frac{1}{2}\sqrt{S - 4m^2}$.

from $P_{cm}$, $E_1 = \frac{1}{2\sqrt{S}}(S + m_1^2 - m_2^2)$ and $E_2 = \frac{1}{2\sqrt{S}}(S + m_2^2 - m_1^2)$.

In this case also, if $m_1 = m_2$, $E_1(cm) = E_2(cm) = \sqrt{S}/2$.

In fixed target frame, $\vec{P}_2 = 0$, $E_2 = m_2$

Implies,

$$S = m_1^2 + m_2^2 + 2E_1 m_2$$

and

$$E_1 = E_{1(kin)} + m_1$$

For high energy experiments, the beams can be of two different energy and at such high energies masses of particles can be neglected. So, from

$$S^2 = (p_1 + p_2)^2 = (E_1 + E_2)^2 - (\vec{P_1}^2 + \vec{P_2}^2)$$

we get,

$$\sqrt{S} \approx \sqrt{4E_1 E_2}$$

# Chapter 7

# Event Qualitative Analysis

The data analysed is obtained from STAR experiment for Au+Au collision at $\sqrt{s_{NN}}$= 200 GeV.

To ensure that the physics deductions obtained from the data is not dependent upon detector descrepancies, we select data only in that region of parameter space ($\eta$, $\phi$) in which detector acceptance and particle detection is uniform.

To select good events, we apply several track cuts and event cuts as follows (Table 7.1):

| **EVENT CUTS** | **TRACK CUTS** |
|---|---|
| $\|V_z\| < 30$ cm | $p_T < 10$ GeV/c |
| Vertex radius $< 2$ cm | $\|$Charge$\|= 1$ e$^-$ |
| TOF Multiplicity $> 2$ | TPC nHitsFit $> 15$ |
| $\|$V$_z$-VPD V$_z\| < 3$ cm | $\|\eta\| < 1$ |
| | $0.52 <$ (nHitsFit/nHitsPossible) $< 1.05$ |
| | $\|$Distance of Closest Approach (DCA)$\| < 1$ cm |

Table 7.1: Selection cuts used in the analysis.

$V_z$ stands for the distance Z projection of the vertex from the point of collision (0,0). We put a $V_z$ cut to select good events all of which emerge from around the same collision point. Also, the $V_z$ cut selects a region in which the detector has uniform coverage. To avoid beam-pipe contaminations, we put a vertex radius cut of 2 cm. For selecting good tracks, we select those tracks with atleast 15 hits in TPC (Time Projection Chamber) and to avoid tracks that might have undergone *Track Splitting* or *Track Merging*, we put the (nHitsFit/nHitsPossible) cut. If one true particle goes through two sectors of TPC and thus gives rise to two different tracks upon recon-

struction, then nHitsFit is less than NHitsPossible. We only take those tracks which do not show splitting beyond 0.52. Similarly, track merging give rise to more number of NHitsFit than NHitsPossible. So we choose tracks only within the above specified range. The $\eta$ range selected here is the region in which the detector acceptance is uniform. For event plane calculation we have taken $0.05< |\eta| <1$ and for flow coefficient calculation, we have taken $|\eta| <0.5$. The multiplicity of an event is taken from the RefMult class provided in the STAR framework which selects tracks with the following cuts: $|\eta| < 0.5$, |DCA| < 3 cm and nHitsFit (TPC)>=10.

We plot all the experimental observables as follows without cuts and with cuts and compare them to confirm that our cuts select events/tracks with minimal detector biases.

Although for QA plots we have shown a $p_T$ <10 GeV cut, for event plane determination and flow coefficient calculations we have used $0.2< p_T <2$ GeV and $p_T <2$ GeV respectively.

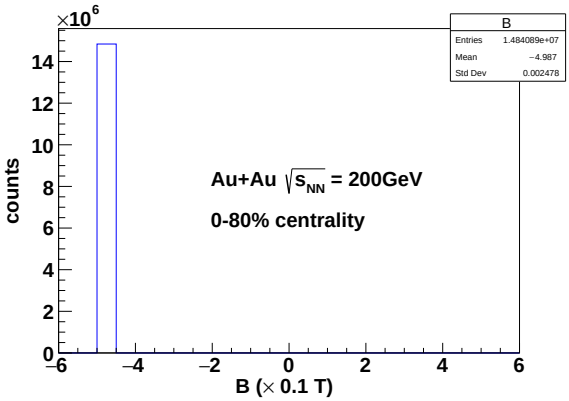


Figure 7.1: Magnetic Field applied for the data taken.

The STAR detector is run at reverse-full field of 0.5 T for the data taken (Fig. 7.1).

In Fig. 7.2, the number of events in each centrality class is shown. After applying

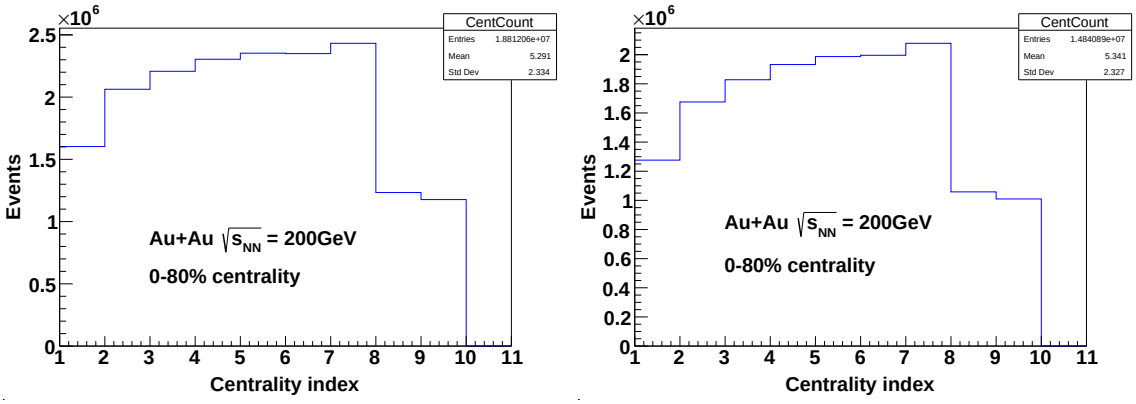


Figure 7.2: Number of events in each centrality before cuts (left) and after cuts (right) are applied.

the cuts, the number of events decreases (Fig. 7.2). In the last two centrality bins, the number of events are small because they are of centrality gap of 5 each (0-5% and 5-10%) while others are of an interval of 10 each. In the most peripheral centrality (70-80%, bin no. 1), the number of events are low due to detector inefficiency.

The number of events in each centrality are as follows after cuts (Table 7.2):

| Centrality | Centrality Bin Number | No. of events |
|---|---|---|
| 0-5% | 9 | 1.0097 $\times 10^6$ |
| 5-10% | 8 | 1.0583 $\times 10^6$ |
| 10-20% | 7 | 2.0780 $\times 10^6$ |
| 20-30% | 6 | 1.9959 $\times 10^6$ |
| 30-40% | 5 | 1.9869 $\times 10^6$ |
| 40-50% | 4 | 1.9323 $\times 10^6$ |
| 50-60% | 3 | 1.8279 $\times 10^6$ |
| 60-70% | 2 | 1.6754 $\times 10^6$ |
| 70-80% | 1 | 1.2762 $\times 10^6$ |

Table 7.2: Number of events in each centrality after applying all the cuts.

In Fig. 7.3, Refmult distribution is shown. The nature of distribution for refmult remains the same before and after the cuts, although a small change is visible for very

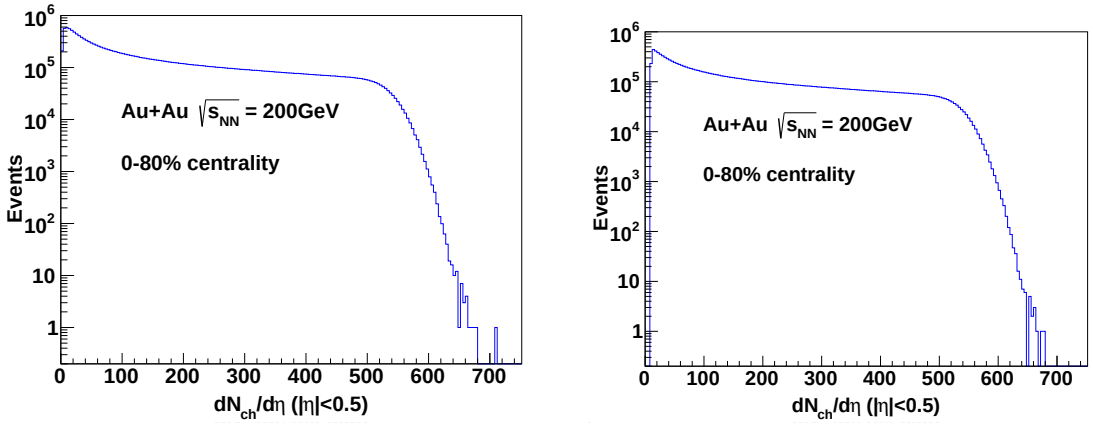


Figure 7.3: Reference Multiplicity before cuts (left) and after cuts (right) are applied.

high and very low values of multiplicity.

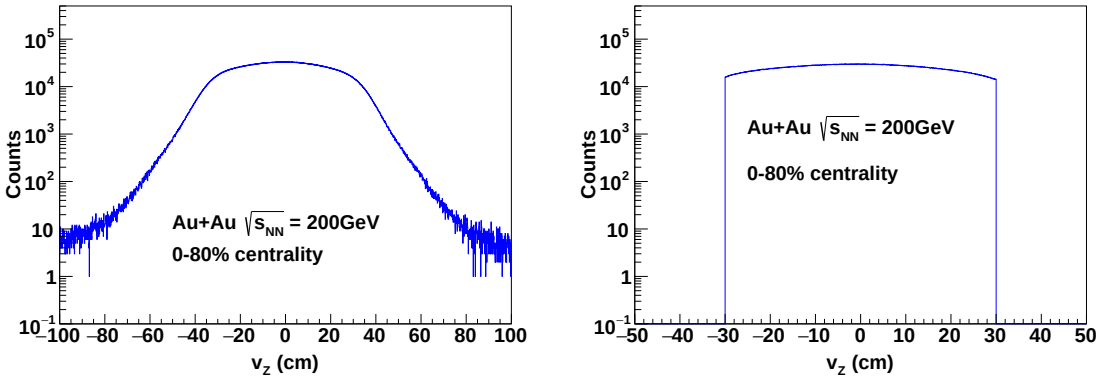


Figure 7.4: Vertex-Z positions before cuts (left) and after cuts (right) are applied.

Vertex-Z denotes the position of the interaction points along beam axis. So, for a good event, most of the interactions should take place near the central region. As there is variation in the distribution before aplying cuts, we choose events within the range in which number of events is uniform (eg. detector coverage is uniform) (Fig. 7.4).

Vertex-X denotes the 'x' position of the interaction points inside beam pipe. So, for a good event, most of the interactions should take place near the central region.

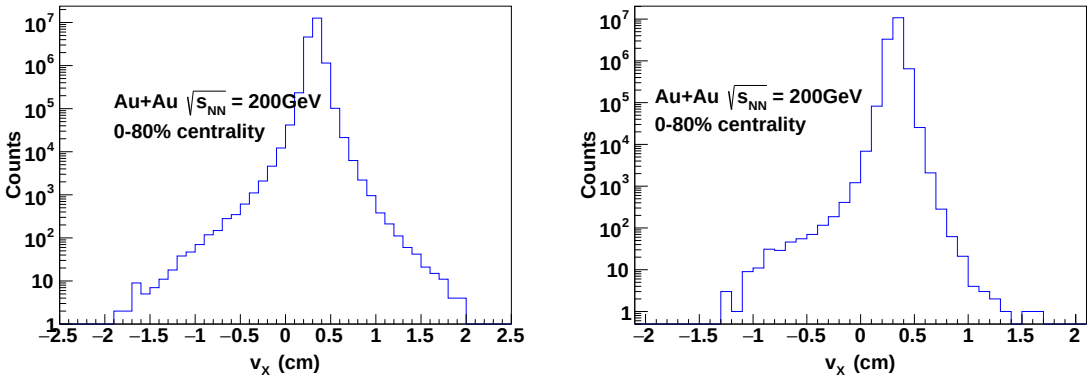


Figure 7.5: Vertex-x positions before cuts (left) and after cuts (right) are applied.

But in this case, the peak can be seen a little away from centre (Fig. 7.5). This implies misallignment of beam with the beam-pipe. For analysis we take only those events which are close to the centre by applying cuts. Also, the vertex-x cut minimises the contamination from beam pipe (of radius=4 cm).

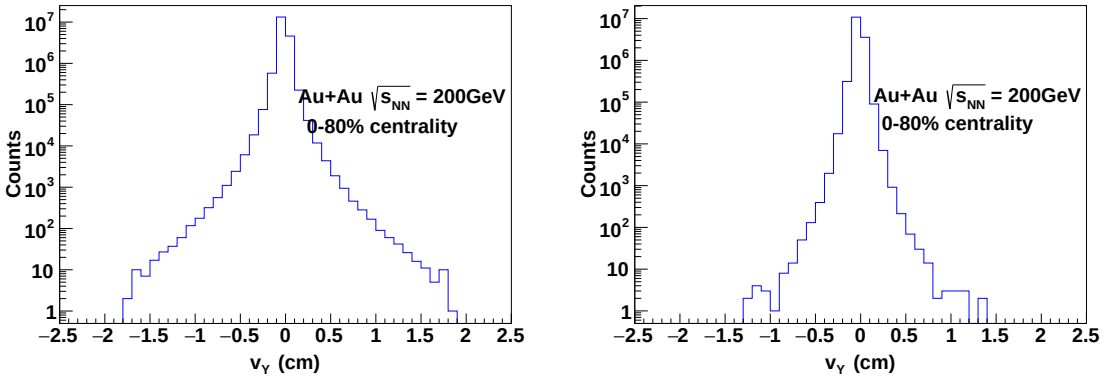


Figure 7.6: Vertex-y positions before cuts (left) and after cuts (right) are applied.

We apply the vertex-y cut for exactly similar reasons for which we apply the vertex-x cut (Fig. 7.6).

As was shown in vertex-x and vertex-y disributions, the beam is misalligned with the beam-pipe axis. This can be clearly noticed in above distribution (Fig. 7.7). For selecting good events, we consider those events whose vertices lie within 2 cm from

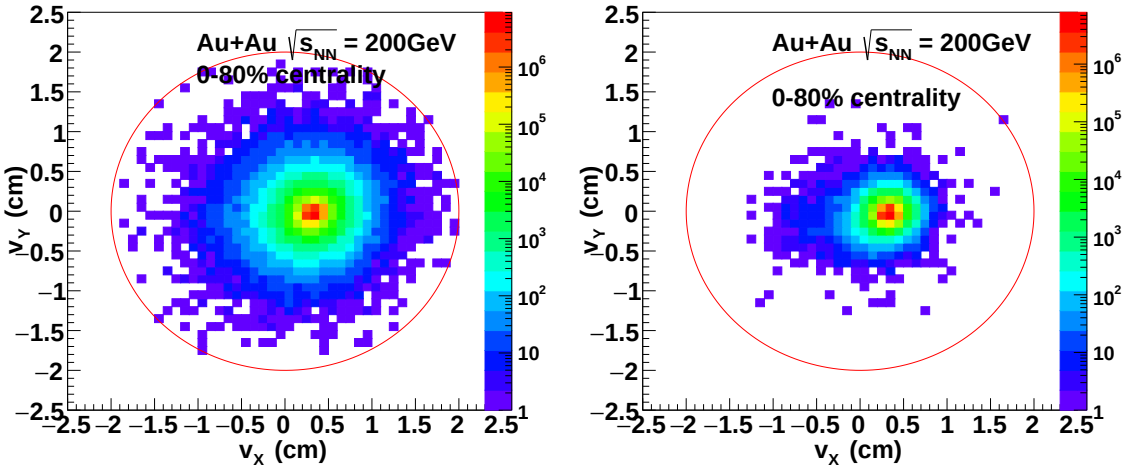


Figure 7.7: Vertex-x position vs vertex-y position before cuts (left) and after cuts (right) are applied.

the beam pipe centre.

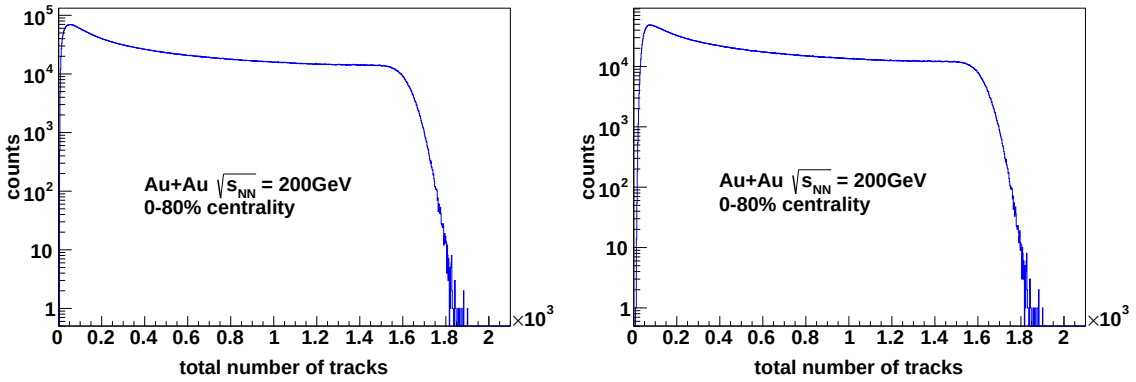


Figure 7.8: Total number of tracks before cuts (left) and after cuts (right) are applied.

As can be seen in Fig. 7.8, the number of tracks with lower count is high as the total energy available for production of the particles is fixed.

From Fig. 7.9, we can observe that higher number of events are with lower Refmult (i.e peripheral) and most vertices lie close to the central position, which is expected. After applying the vertex-z cut, we exclude events which happen away from the central

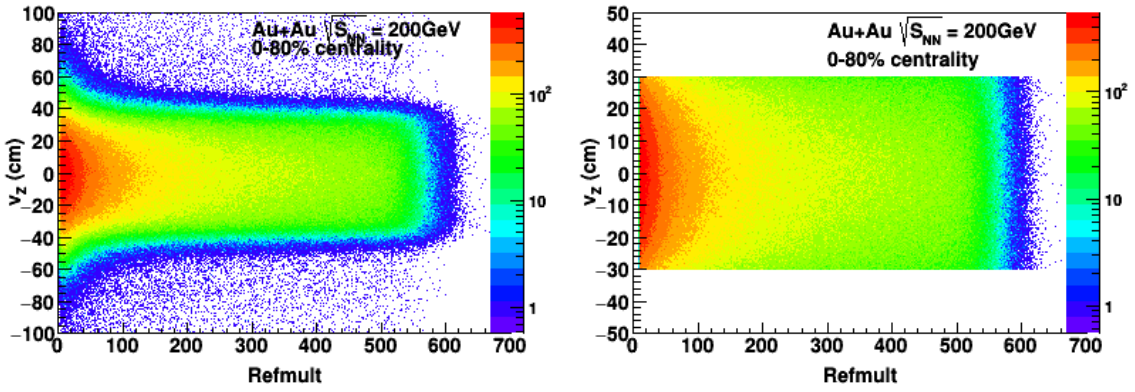


Figure 7.9: Refmult Vs vertex-z position before cuts (left) and after cuts (right) are applied.

position.

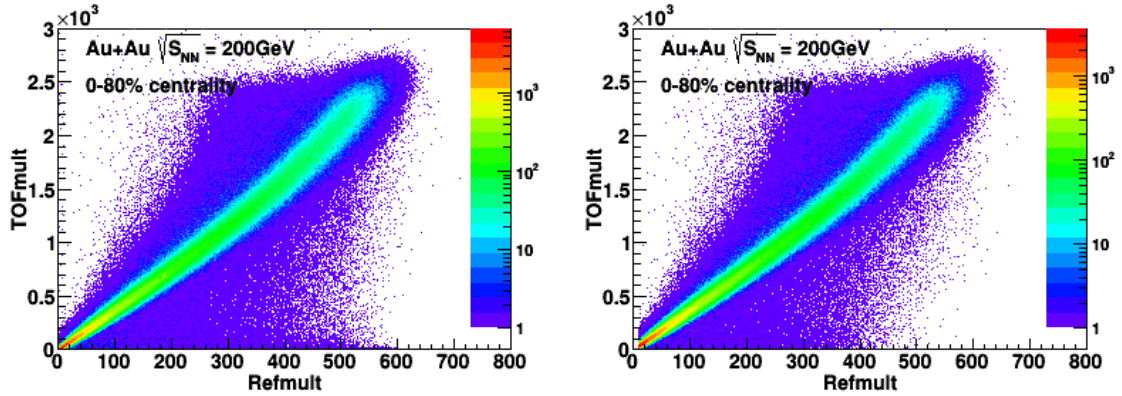


Figure 7.10: Refmult vs TOFmult before cuts (left) and after cuts (right) are applied.

There should be a strictly linear correlation between the Refmult (from TPC) and multiplicity obtained from Time of Flight (TOF) detector. By applying cuts we exclude most of those events which show deviation from the expected linearity (Fig. 7.10).

Just like Vertex-Z distribution, we apply the VPD $V_z$ cut to select events within the range in which the VPD (Vertex Position Detector) coverage for the determination of the vertex position is almost uniform(Fig. 7.11).

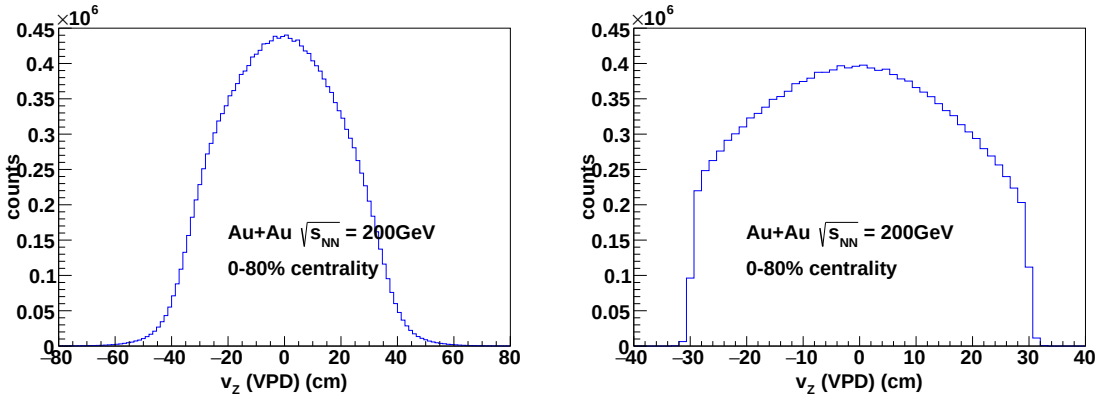


Figure 7.11: Vertex Z position from VPD before cuts (left) and after cuts (right) are applied.

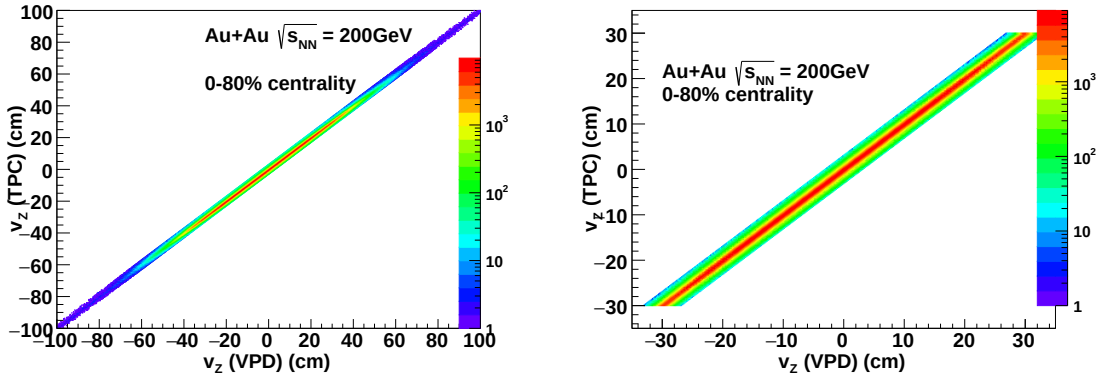


Figure 7.12: Vpd-$v_Z$ vs Vertex Z position from TPC hits reconstruction before cuts (left) and after cuts (right) are applied.

Values of Vertex-Z positions obtained from TPC and VPD should match strictly in the ideal case and we should expect a linear behaviour. By applying ($V_z$-VPD $V_z$) cut we exclude those events which show large deviations from the expected linearity (Fig. 7.12).

Calorimeter measurements are categorised as "destructive measurements" as the particle deposits all its energy inside the calorimeter.

The zero degree calorimeter measures the energy deposited by incident spectator nucleons. This is also called ZDC response. As spectators move in both direction

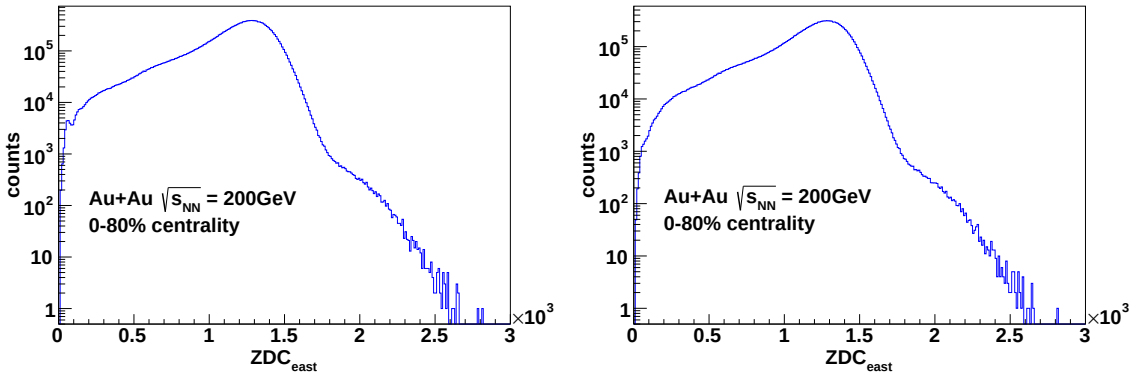


Figure 7.13: Left going spectator neutrons before cuts (left) and after cuts (right) are applied.

along the z-axis, ZDC are situated at both ends of the detector to measure left and right going spectators.

After cuts the number of events decrease but the nature of distribution remains the same for left going neutrons(Fig. 7.13).

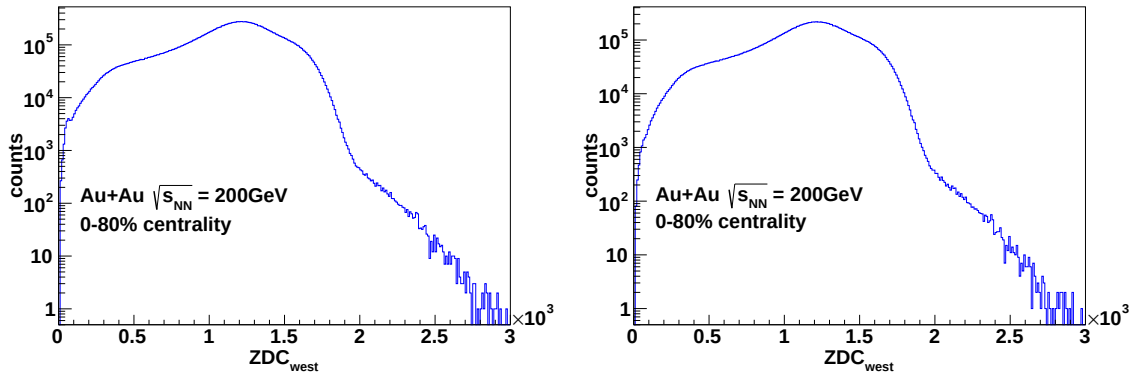


Figure 7.14: Left Going spectator Neutrons before cuts (left) and after cuts (right) are applied.

Just like left going neutrons we expect a similar behaviour for right going neutrons (Fig. 7.14).

Fig. 7.15 corresponds to the total number of spectator nucleons which is similar in nature to both left and right going neutrons individually.

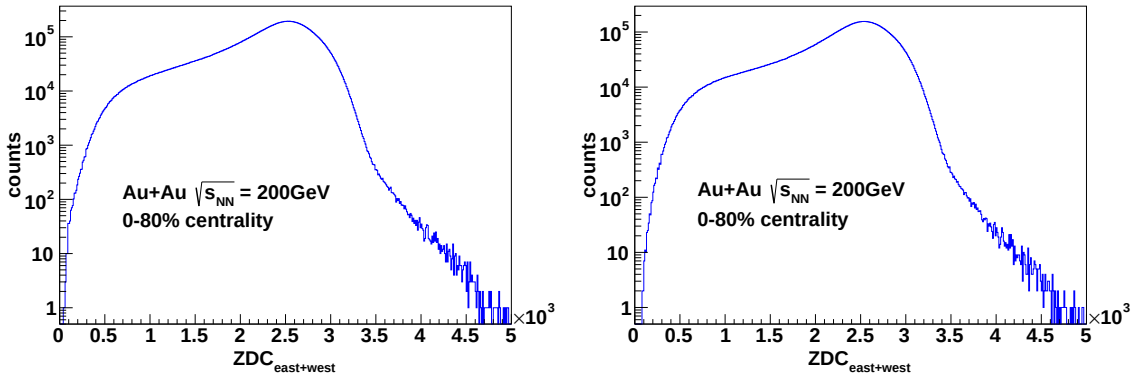


Figure 7.15: Total number of Spectator neutrons (east going+west going) before cuts (left) and after cuts (right) are applied.

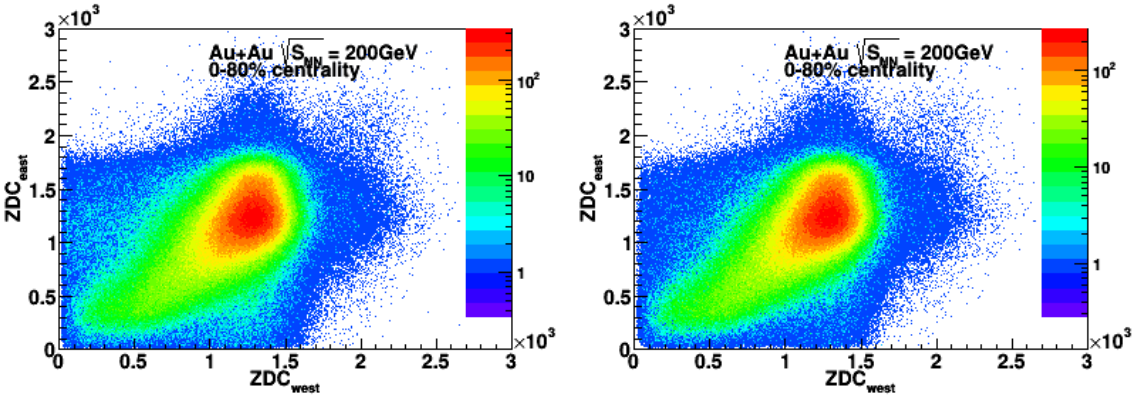


Figure 7.16: Left going spectator neutrons vs right going spectator neutrons from ZDC before cuts (left) and after cuts (right) are applied.

From Fig. 7.16 it can be observed that the number of spectators incident on the left and the right ZDC detector follow an approximately linear trend as expected. As total number of nucleons in a nucleus is fixed, approximately equal number of spectators are expected to be incident on both detectors for a given event.

From Fig. 7.17 it can be observed that as the number of spectators decrease, multiplicity increases. This happens because the number of nucleons in a nucleon is fixed and for high-multiplicity events more nucleons will have to interact leaving only a few spectators. By applying cuts, we want to reduce the number of such events

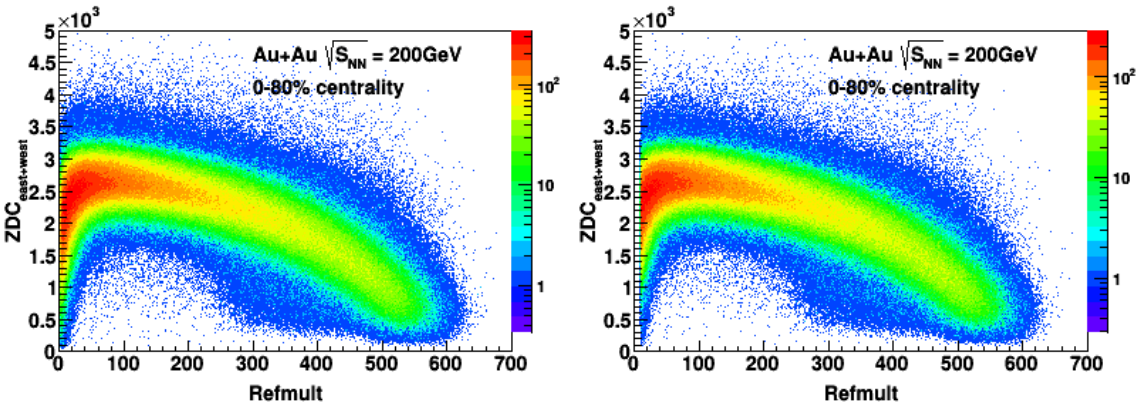


Figure 7.17: Refmult vs spectator neutrons count (from ZDC) before cuts (left) and after cuts (right) are applied.

which show lower multiplcity with lower number of spectators.

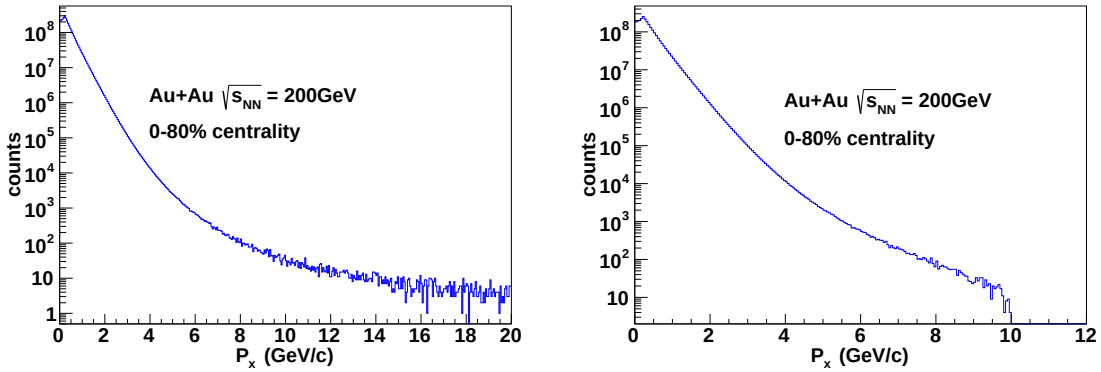


Figure 7.18: $P_x$ distribution before cuts (left) and after cuts (right) are applied.

The number of particles with higher momentum along x direction is low and lower momentum is high (Fig. 7.18) as there is only a fixed amount of energy available to be taken away by produced particles.

The number of particles with higher momentum along y is low and lower momentum is high (Fig. 7.19) as there is only a fixed amount of energy available to be taken away by produced particles.

The number of particles with higher momentum along Z is low and lower momen-

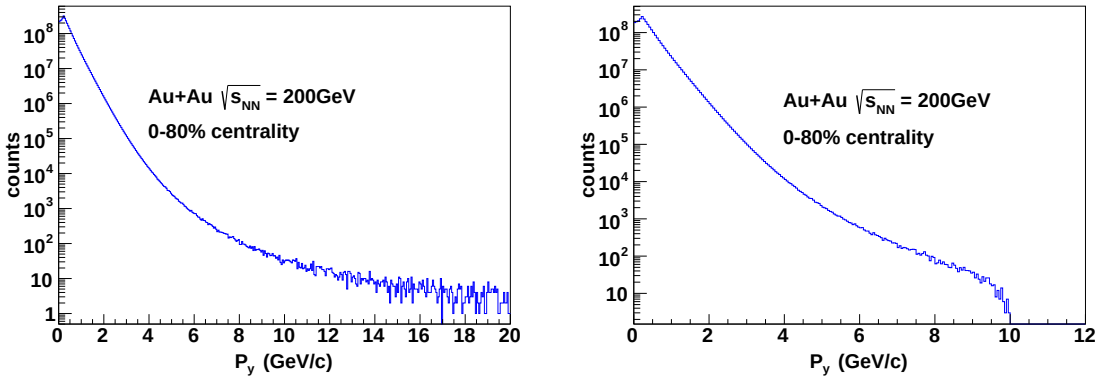


Figure 7.19: $P_y$ distribution before cuts (left) and after cuts (right) are applied.

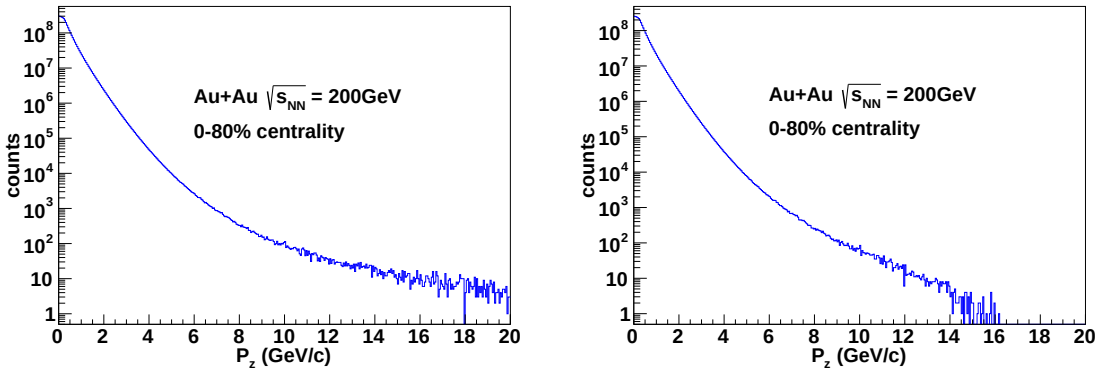


Figure 7.20: $P_z$ distribution before cuts (left) and after cuts (right) are applied.

tum is high (Fig. 7.20) as there is only a fixed amount of energy available to be taken away by produced particles.

Fig. 7.21 shows that the particle production in the transverse plane is almost uniform. The 12 sectors of the TPC detector can be clearly seen.

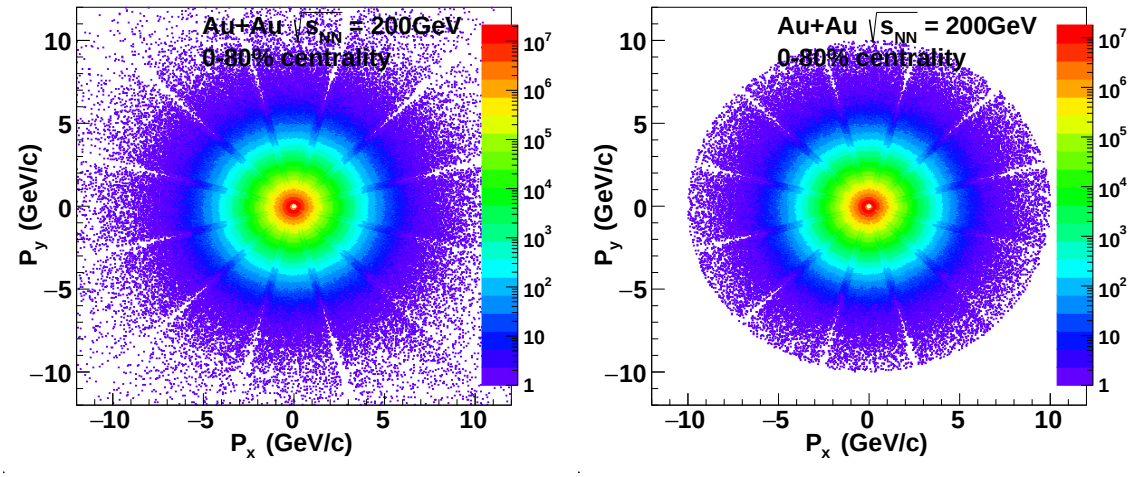


Figure 7.21: $P_y$ vs $P_x$ before cuts (left) and after cuts (right) are applied.

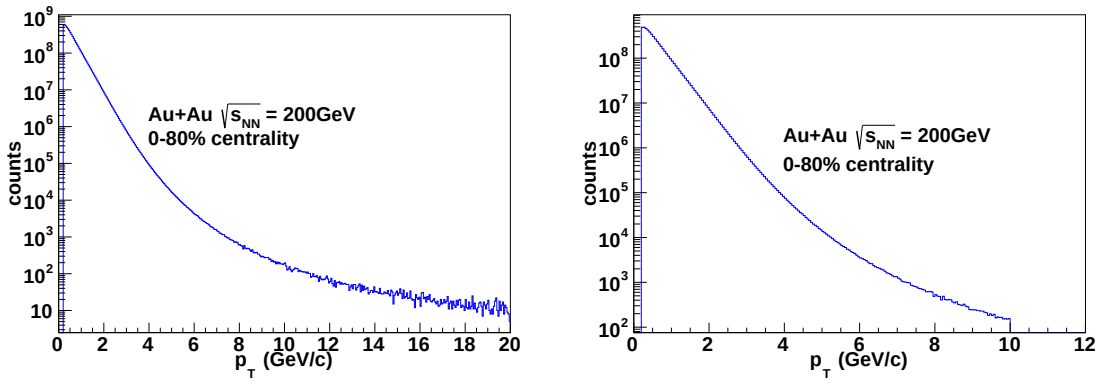


Figure 7.22: Transverse Momentum distribution before cuts (left) and after cuts (right) are applied.

$$p_T = \sqrt{P_x^2 + P_y^2}$$

The number of particles in transverse plane with higher momentum is low and lower momentum is high (Fig. 7.22) as there is only a fixed amount of energy available to be taken away by produced particles. The cut limits the momentum in transverse plane upto a value of 10 GeV.

A low $p_T (> 0.2$ GeV) cut is applied to reduce non flow contributions coming from

resonance decays and to remove inefficiency of TPC. The high $p_T$($<$ 10 GeV or $<$ 2 GeV) cut is applied to reduce non-flow contributions coming from jets.

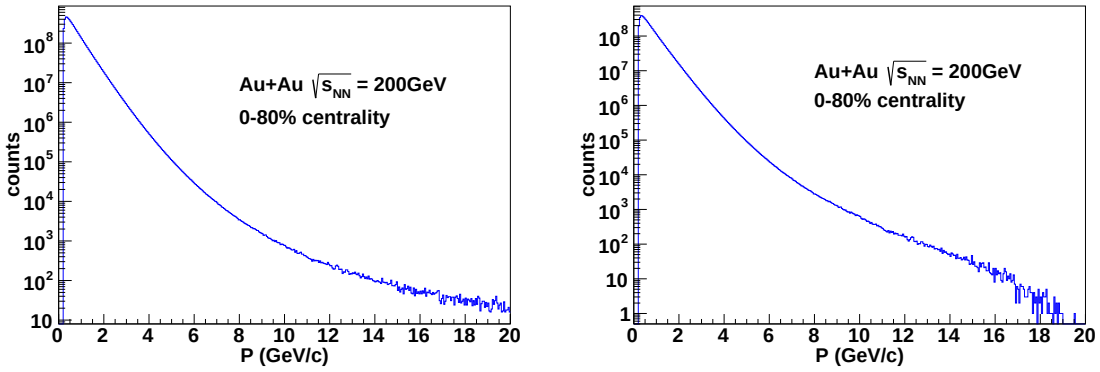


Figure 7.23: Total Momentum (P=$\sqrt{P_x^2 + P_y^2 + P_z^2}$) before cuts (left) and after cuts (right) are applied.

The total momentum distribution displays similar nature as $P_x$, $P_y$, $P_z$ or $p_T$ (Fig. 7.23).

The $P_x$, $P_y$, $P_z$, $p_T$ and total momentum distributions follow an exponential distribution in the lower momentum limit and a power law distribution in the higher momentum limit.

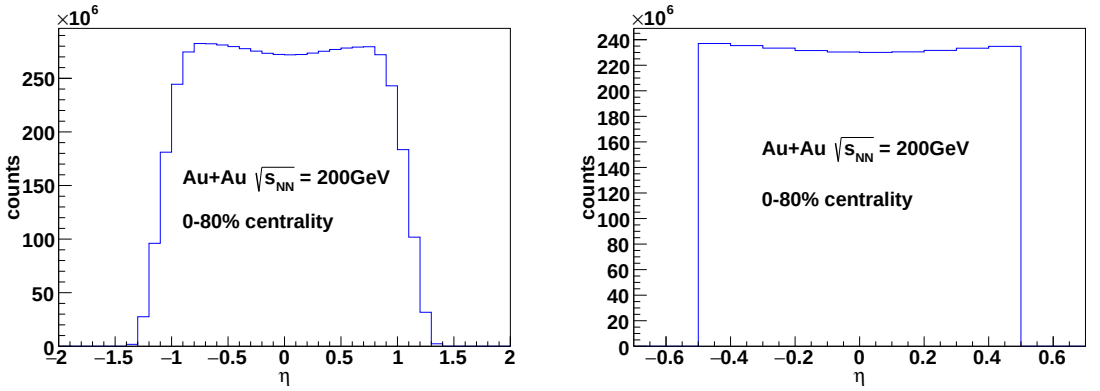


Figure 7.24: Pseudorapidity ($\eta$) before cuts (left) and after cuts (right) are applied.

$$\eta = ln(\frac{P + P_z}{P - P_z})$$

We put a pseudorapidity cut to select only those particles which are produced within $|\eta| < 1$ because the detector acceptance is uniform in this range (Fig. 7.24).

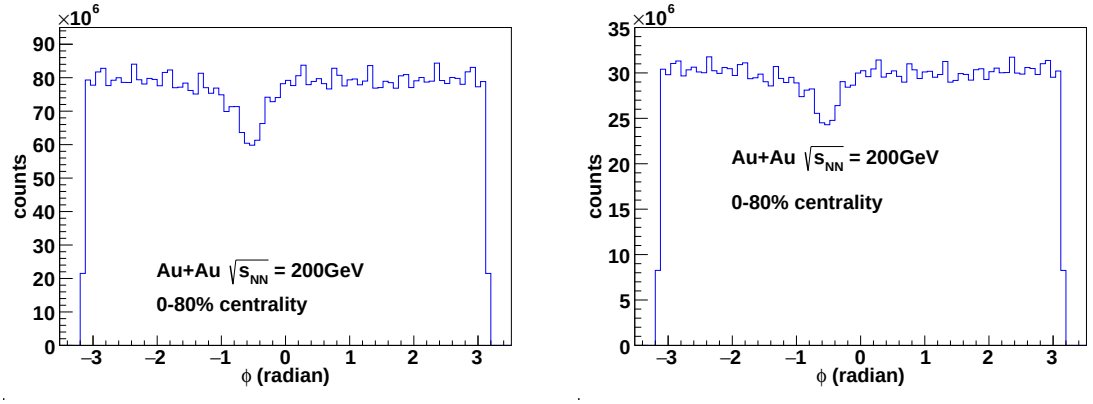


Figure 7.25: $\phi$ distribution before cuts (left) and after cuts (right) are applied.

$$\phi = tan^{-1}(\frac{P_y}{P_x})$$

The azimuthal angle distribution of particles should be uniform throughout(as seen from $P_x$ vs $P_y$ distribution (Fig. 7.21)). But the dip observed in the $\phi$ distribution (Fig. 7.25) can be attributed to detector malfunctioning.

$$\theta = cos^{-1}(\frac{P_z}{P})$$

We observe the dip in the middle close to $\pi/2$ because it corresponds to the beam direction. Most of the particles are produced in the transverse plane and their number decreases as we move towards the beam direction (Fig. 7.26).

From Fig. 7.27, it is re-emphasized that the $|\eta|$ cut provides us with a region of uniform particle production. By applying cuts we also overcome the non-uniformness of particle production in $\phi$.

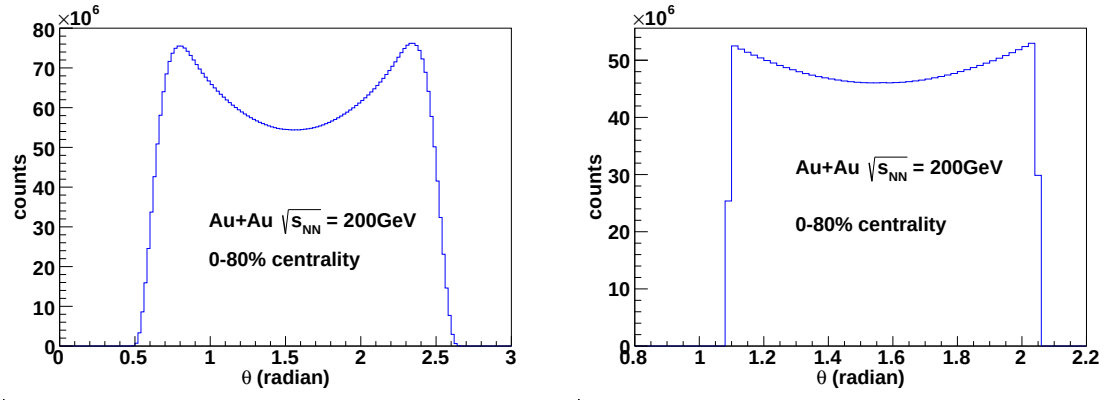


Figure 7.26: $\theta$ distribution before cuts (left) and after cuts (right) are applied.

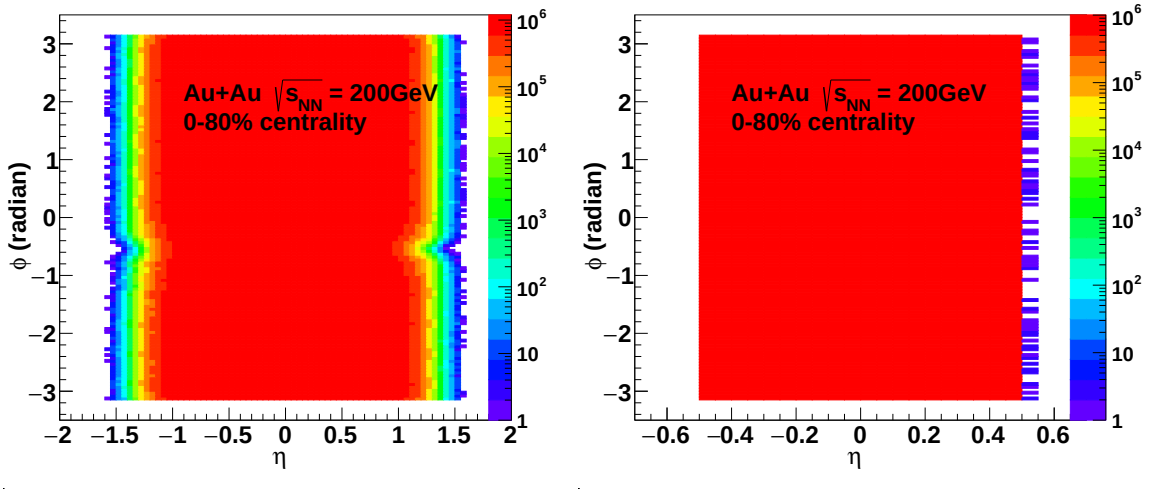


Figure 7.27: $\eta$ vs $\phi$ distribution before cuts (left) and after cuts (right) are applied.

Both $|\eta|$ and $p_T$ cut provide us an optimum range in which the detector acceptance is uniform and the non-flow contributions are minimised (Fig. 7.28).

$$-\frac{dE}{dx} \propto [1 + \frac{m^2}{P^2}]$$

dE/dx plots provide the ionisation energy loss with unit distance (from Bethe- Bloch formula) and are useful to identify particles present in the analysis. For a given momentum, particles of different mass experience different ionisation losses. Thus

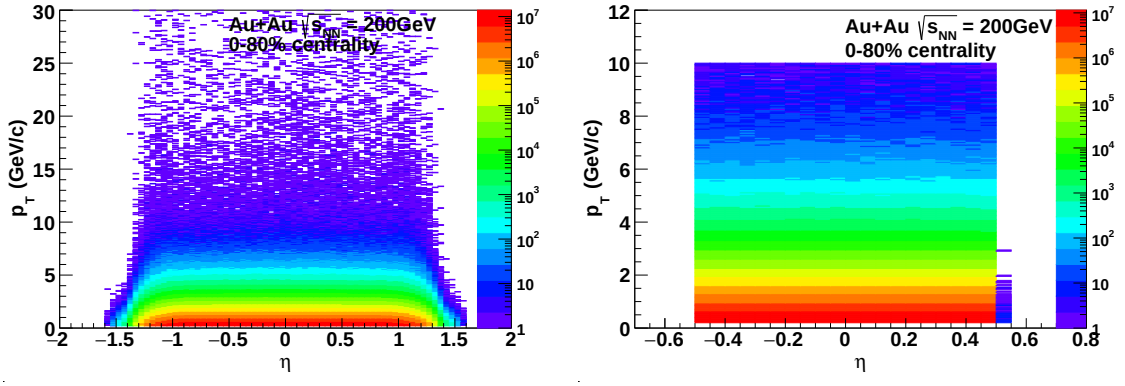


Figure 7.28: $\eta$ vs $p_T$ distribution before cuts (left) and after cuts (right) are applied.

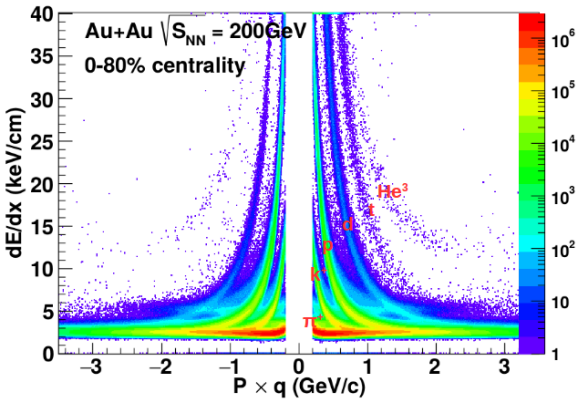


Figure 7.29: $\frac{dE}{dx}$ vs P×q (rigidity) distribution for particle identification (with all the cuts).

different particles form different bands in Fig. 7.29. In figure 7.29, starting from the bottom (right half), the lines denote bands for pion, kaon, proton, deuteron, tritum, $He^3$ etc. The bands on the left half correspond to the respective anti-particles.

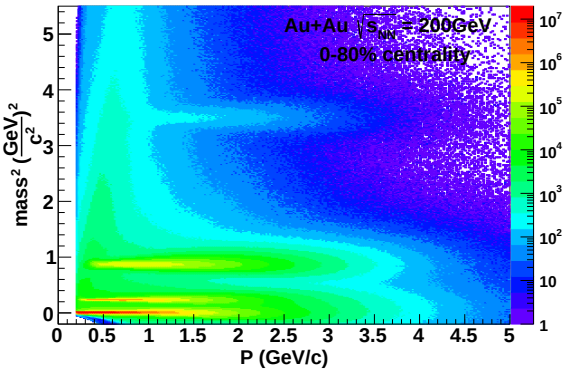


Figure 7.30: Mass$^2$ vs momentum distribution for particle identification (with cuts).

Fig. 7.30 shows bands for different particles such as (starting from bottom) electron, pion, kaon, proton and deuteron. The identification can be done owing to the mass of particles and can be thus verified regarding which band belongs to which particle.

p=$\gamma mv \implies \frac{p}{c} = \frac{\gamma mv}{c} = \gamma m\beta$.

So, $m^2 = \frac{p^2}{c^2\gamma^2\beta^2}$.

Also, $\frac{1}{\gamma^2\beta^2} = \frac{1}{\beta^2} - 1$.

Therefore,$m^2 = \frac{p^2}{c^2}(\frac{1}{\beta^2} - 1)$. We get value of momentum from TOF and $\beta = v = \frac{\Delta L}{\Delta T}$ is obtained from TOF, where $\Delta L$ is the length traversed in TOF chamber and $\Delta T$ is the time taken for traversing the distance $\Delta L$.

TOF detector gives $m^2$ vs $p_T$ distributions which we use to identify the particles present in our analysis.

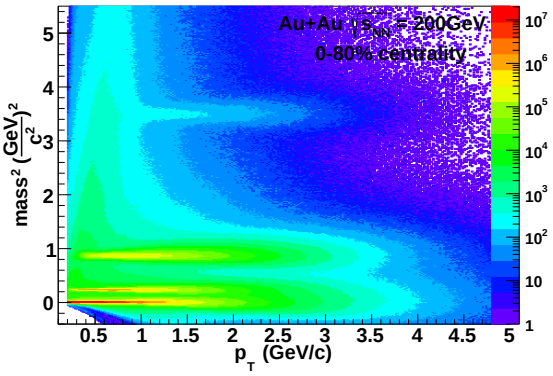


Figure 7.31: Mass$^2$ vs $p_T$ distribution for particle identification (with cuts).

Fig. 7.31 is just like the previous particle identifiction (PID) figures, except that the bands in this figure is clearer to observe. In this plot too we can identify the particles detected in our experiment.

# Chapter 8

# Data Analysis

The data for Au+Au collision at $\sqrt{s_{NN}}$= 200 GeV was obtained from STAR (Run 11 data) experiment and is analysed in this work. 14.92 million events were analysed. The multiplicity used in further analysis is not corrected for efficiency.

For calculating the $v_2$ in the eta-sub event plane method, the $\eta$ range (-1< $|\eta|$ <1) was divided into two groups with almost equal number of tracks with a gap of $\Delta\eta$= 0.1. The event plane for both regions were then calculated namely $\psi_{2east}$ for the negative $\eta$ range and $\psi_{2west}$ for the positive $\eta$ range (for second harmonic).

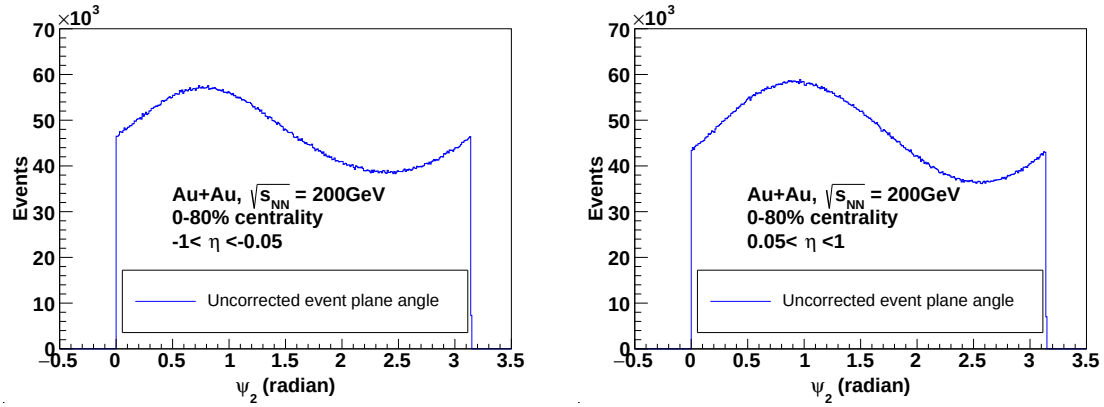


Figure 8.1: $\psi_{2east}$ and $\psi_{2west}$ distribution.

The event plane is expected to be perfectly horizontal owing to the randomness in the impact parameter of individual collision events . But as can be seen from Fig. 8.1, it is not, due to detector inefficiency. So, to account for it and make it flat, recentering correction was applied, i.e subtracting the mean value of $Q_x$ and $Q_y$, the x and y components of the flow vector, from individual values of $Q_x$ and $Q_y$ on an event by event basis. Then these corrected values were used to calculate event plane

angle.

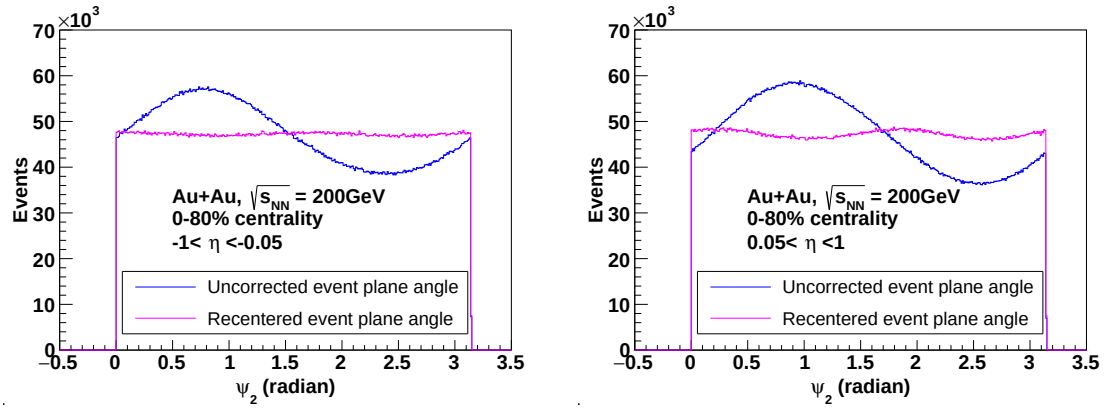


Figure 8.2: Recenter corrected $\psi_{2east}$ and $\psi_{2west}$.

The shortcoming in recenter correction is that the contribution from higher harmonics still do not get removed (Fig. 8.2). So, shift correction was used as decribed earlier (Fig. 8.3).

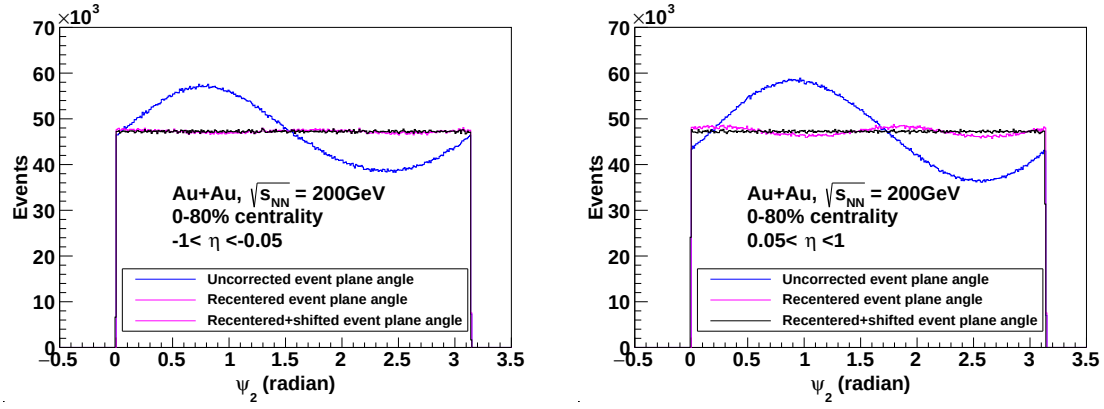


Figure 8.3: Shift corrected event planes for both the $\eta$ ranges.

To check for the flatness of the corrected event plane, it was we fitted with the function $p_0(1+p_1.cos(2x)+p_1.sin(2x))$ and for a perfectly flat event plane, the order of magnitude of $p_0.p_1$ and $p_0.p_2$ are expected to be of order 1.

The magnitude of $|p_0.p_1|$ and $|p_0.p_2|$ are observed to be of order 1 in both the sub-eta ranges (Fig. 8.4). So these values of event plane angle are flat enough to be

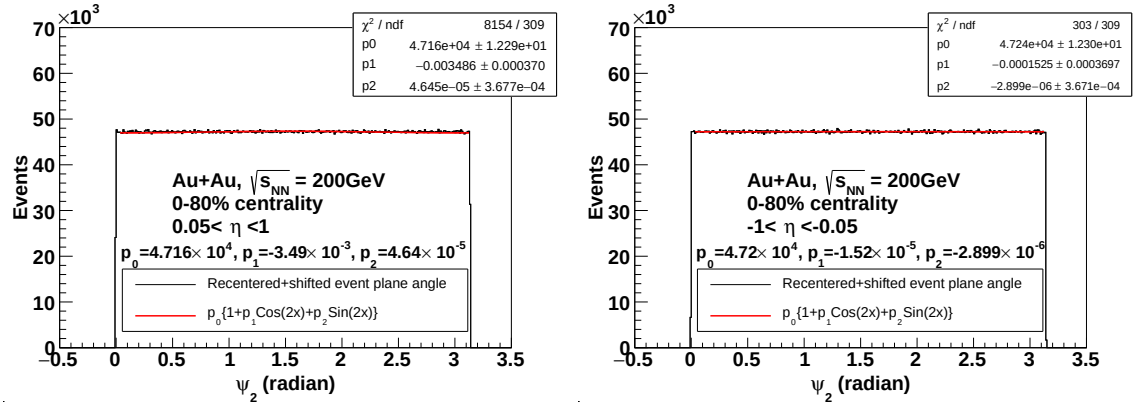


Figure 8.4: Flattened event plane fitted to the function and the parameters are shown on the top.For $\psi_{2east}$, $|p_0.p_1|$= 16.46 and $|p_0.p_2|$= 2.19 and for $\psi_{2west}$, $|p_0.p_1|$= 7.18 and $|p_0.p_2|$= 0.137.

used to calculate $v_2$.

The resolution obtained for different centralities and used throughout the calculation of $v_2$ is shown in Fig. 8.5. The resolution value is observed to be increasing initially with the number of tracks (going from right to left). But, as the collision region becomes more and more spherical with decreasing centrality values, pinpointing the $\phi$ for the particular track becomes more difficult, hence the resolution decreases.

The calculated values of $\psi_2$ resolution from data varies from published result by 3% within errors [15].

Similarly, for calculating $v_3$, the $\psi_3$ was first calculated and recenter and shift corrections were applied (Fig. 8.6). $v_3$ was calculated using the corrected value for $\psi_3$.

Just like for $\psi_2$, the linearity of $\psi_3$ was checked in both $\eta$ ranges (by fitting it with $p_0(1 + p_1.cos(3x) + p_1.sin(3x))$) and was ensured that it is flat before doing further analysis:

The magnitude of $|p_0.p_1|$ and $|p_0.p_2|$ are observed to be of order 1 in both the sub-eta ranges (Fig. 8.7). So, this value of event plane angle is flat enough to be used

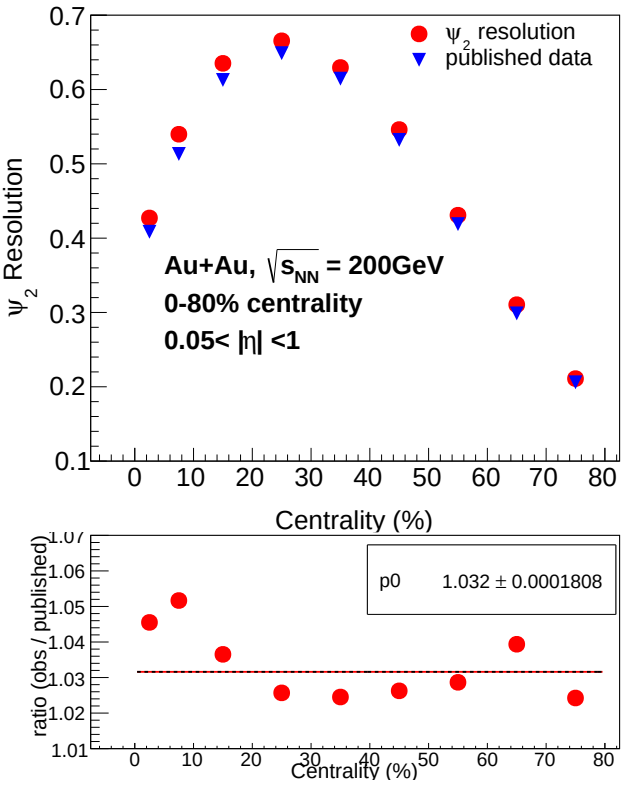


Figure 8.5: $\psi_2$ resolution in different centralities and comparison with published data.

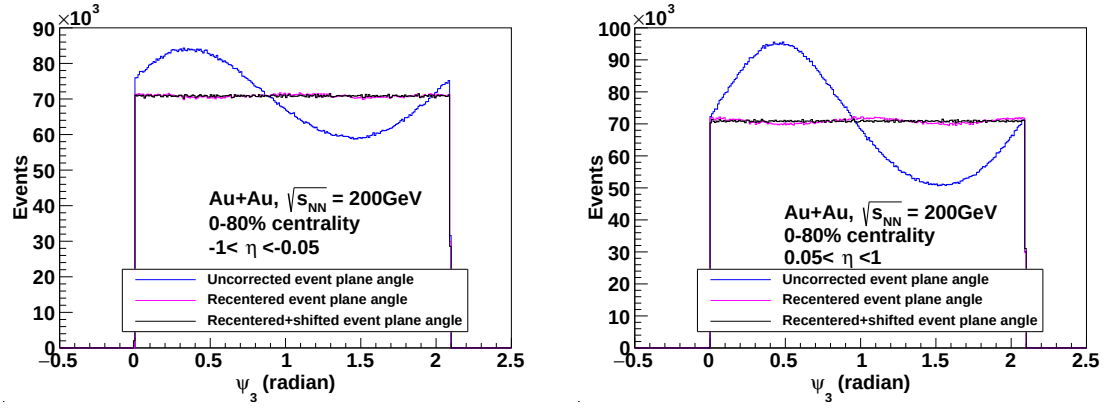


Figure 8.6: $\psi_{3east}$ and $\psi_{3west}$ distribution after applying recenter and shift correction.

to calculate $v_3$.

The $\psi_3$ resolution values obtained for different centralities are shown in Fig. 8.8:

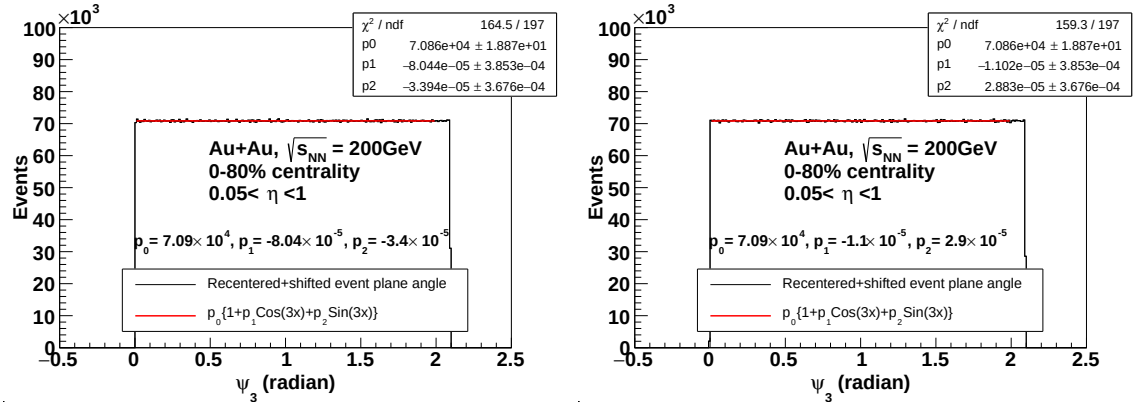


Figure 8.7: Flattened event plane fitted to the function and the parameters are shown on the top.For $\psi_{3east}$, $|p_0.p_1|= 5.7$ and $|p_0.p_2|= 2.4$ and for $\psi_{3west}$, $|p_0.p_1|= 0.78$ and $|p_0.p_2|= 2.0561$.

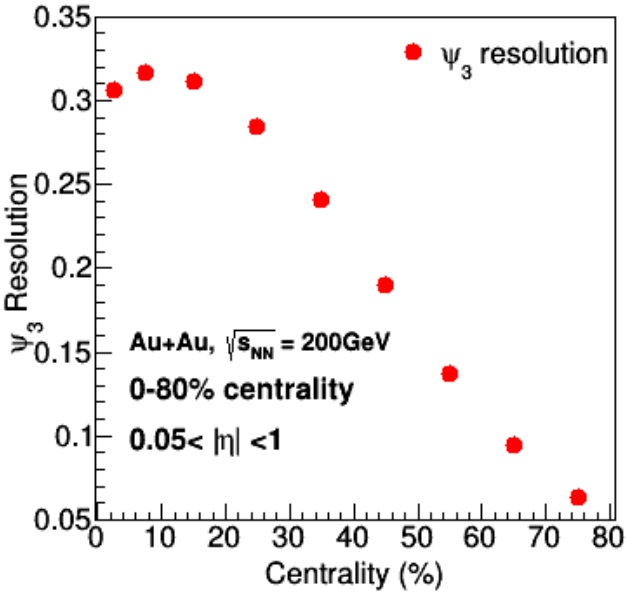


Figure 8.8: $\psi_3$ resolution values in each centrality.

Next, $v_2$ vs $p_T$ and $v_3$ vs $p_T$ was plotted using the values obtained for resolution for different centralities and different L+R bins.

The value of $v_2$ is expected to increase initially before becoming flat. This is expected because high $p_T$ particles are produced early in the collision system and

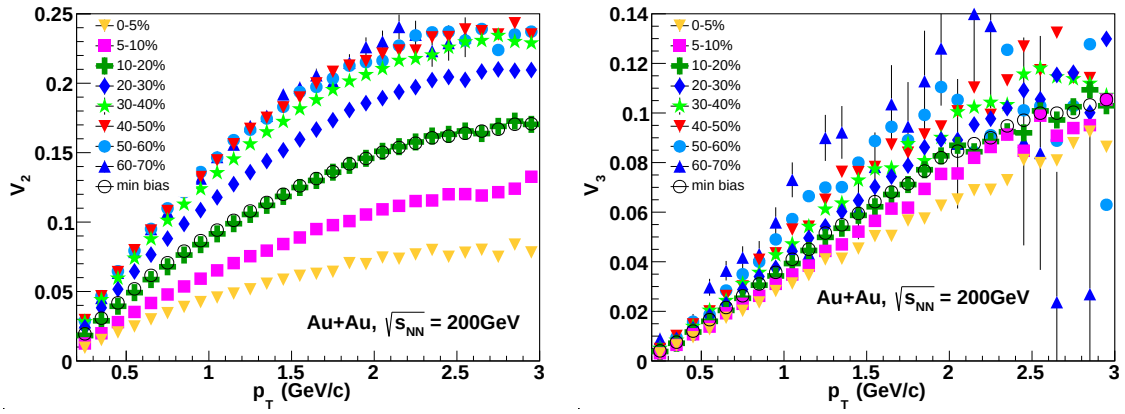


Figure 8.9: Left: $v_2$ vs $p_T$ plot, Right: $v_3$ vs $p_T$ plot for different centralities and minimum bias.

hence can't experience the collectivity. Also, we have the functional dependence from hydrodynamic calculations [16].

$$v_2 \propto (p_T - vm_T)$$

where, $m_T^2 = m^2 + p_T^2$. From this functional dependence we expect the plot to show a rise at low $p_T$, followed by a maxima at intermediate $p_T$ and drop to zero for higher $p_T$ values.

The value of $v_2$ is observed to be increasing as $p_T$ increases until about 3GeV/c, before it starts to drop (Fig. 8.9). The $v_2$ shows a strong centrality dependence whereas it is not so for $v_3$. Because $v_3$ arises from fluctuations in initial state, the values of $v_3$ for 0-5% centrality can be observed to be higher than the values of $v_2$ for 0-5% centrality (Fig. 8.9).

The calculated values for $v_2$ vs $p_T$ in minimum bias was compared with the published data [17] and was found out to be agreeing well with it (Fig. 8.10).

In $v_2$ vs $\eta$ and $v_3$ vs $\eta$ distributions, the effects of $v_n$ is expected to be most

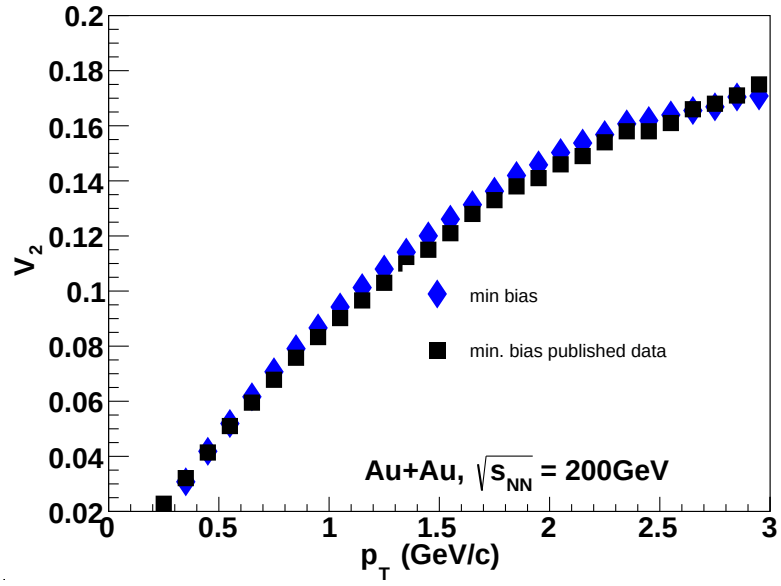


Figure 8.10: Minimum bias $v_2$ vs $p_T$ compared with the published data [17].

pronounced in the transverse plane, i.e for $\eta$=0.

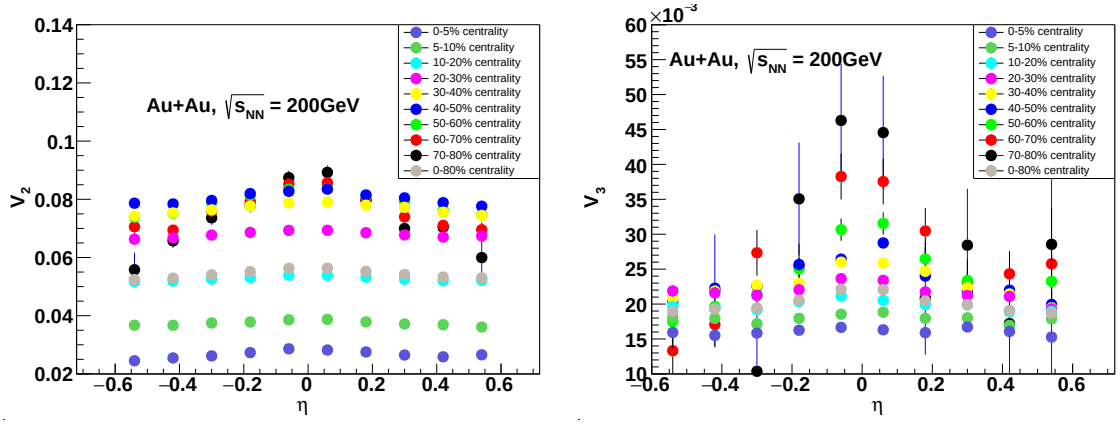


Figure 8.11: Left: $v_2$ vs $\eta$, Right: $v_3$ vs $\eta$ for different centralities and minimum bias.

As can be inferred from Fig. 8.11, the value of $v_2$ and $v_3$ in all the centralities is highest at $\eta = 0$ and decreases as we move away from the centre.

The minimum bias L+R distribution was taken and the L+R distribution for each centrality was extracted (using multiplicity cuts for centrality definition) (Fig. 8.12).

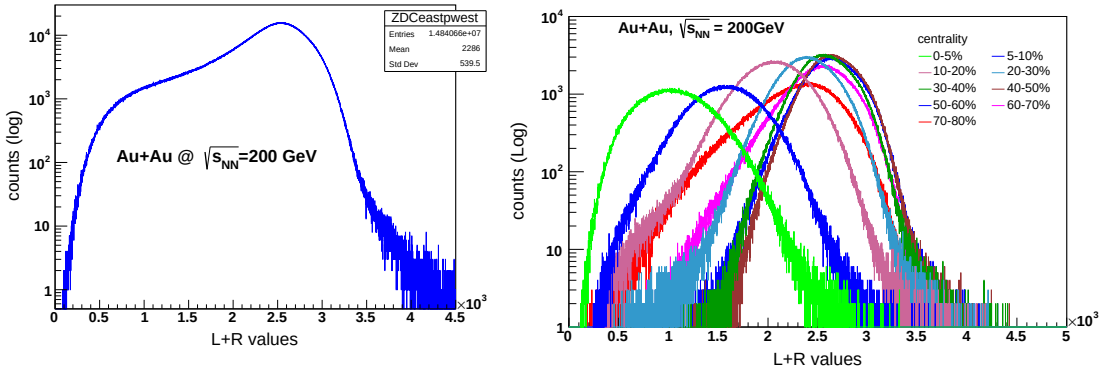


Figure 8.12: Left: The L+R distribution for minimum bias, Right: The spectator distribution for each centrality (by multiplicity) being shown in different colors.

The minimum bias distributions for $v_2$ vs charged particle multiplicity and $v_2$ vs total spectator neutrons (ZDC) are as follows (Fig. 8.13):

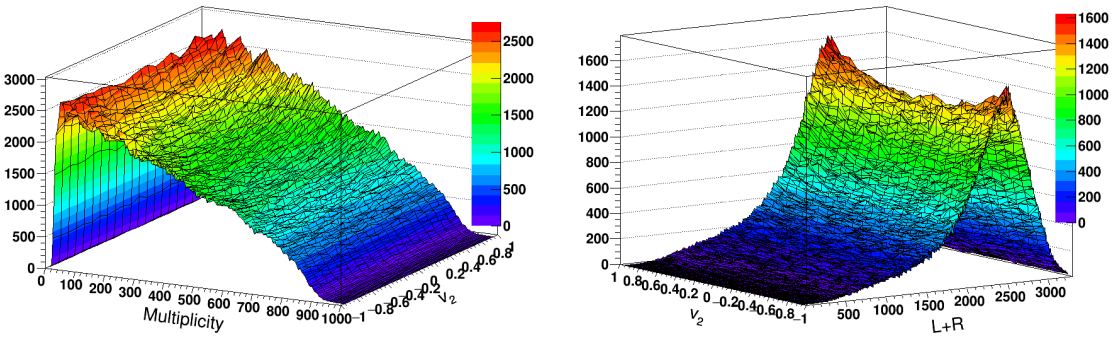


Figure 8.13: Left: $v_2$ vs charged particle multiplicity, Right: $v_2$ vs Spectator Neutrons for all events.

During categorisation of the events into centrality classes, the corresponding distribution in a centrality (10-20% shown as an example) is as follows (Fig. 8.14):

While taking centrality averages of different experimental observables or initial conditions such as $v_n$, multiplicity or $\epsilon_2$, $N_{part}$, the different characteristics that dif-

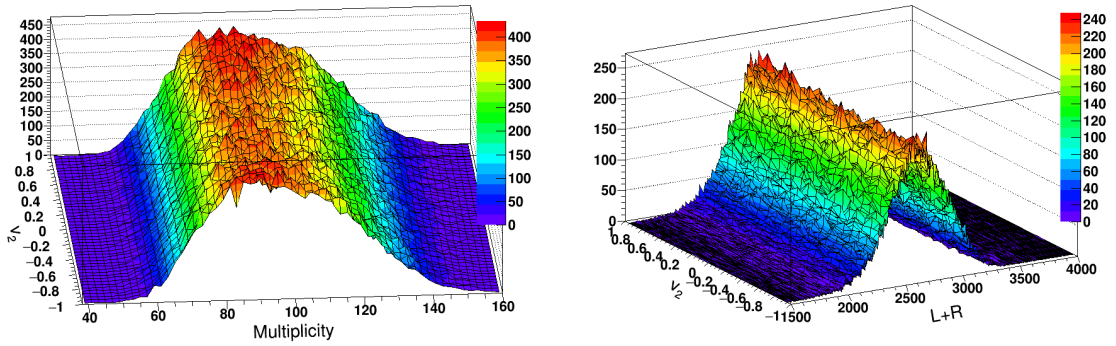


Figure 8.14: Left: $v_2$ vs Multiplicity, Right: $v_2$ vs L+R for 10-20% centrality.

ferent events have in a centrality gets averaged, resulting in a loss of valuable information. This can be verified from Fig. 8.14.

Therefore to investigate the events more deeply, the L+R distribution for each centrality was further divided (by multiplicity) on the basis of L+R (total number of spectator neutrons) values in bins of 0-5%, 5-10%,10-20%, ... 70-80% and 80-100% each (Fig. 8.15). The 0-5% bin is the first shaded bin from left in the L+R distribution for each centrality (Fig. 8.15). Because the L+R distribution corresponds to the calorimetric response coming from spectator neutrons and we can only obtain the total number of spectator nucleons from Glauber model, we have chosen the % binning (of L+R distribution for each centrality) to ensure that we select corresponding events from data and Glauber model for further analysis.

As can be seen in Fig. 8.16, the resolution varies differently in subsequent L+R binning after centrality binning. The $\psi_2$ resolution values show an increasing trend with increasing L+R for 0-5%, 5-10%, 10-20% and 20-30% while it remains almost constant for all subsequent centralities. For $\psi_3$, the values for resolution remains almost a constant for all subsequent centralities starting from 10-20%. For 0-5% and 5-10% centralities the $\psi_3$ resolution increases with increasing L+R.

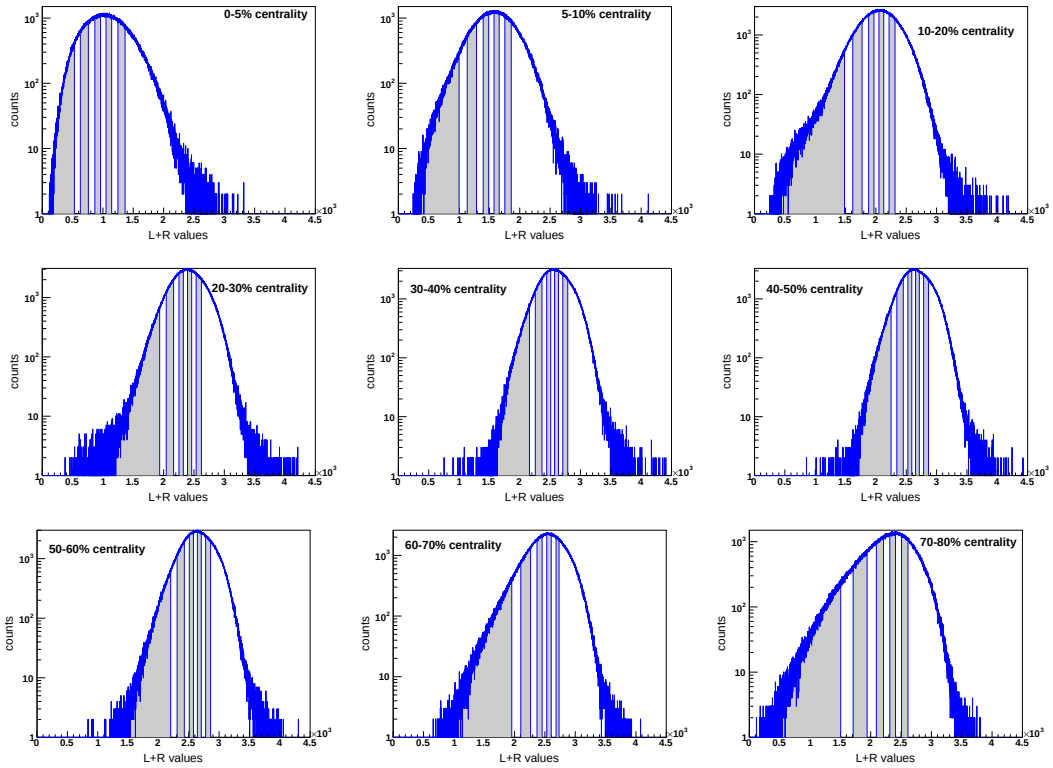


Figure 8.15: The % binning of L+R distribution in each centrality (by multiplicity).

The multiplicity is generally expected to decrease with increasing spectator numbers. But upon plotting charged particle multiplicity for each L+R bin in each centrality, it was observed that the multiplicity decreases with increasing number of spectators for 0-5%, 5-10%,...40-50% but increases with increasing spectator number in the subsequent centralities (Fig. 8.17). This observation is for charged particle multiplicity uncorrected for inefficiencies.

The $v_2$ vs multiplicity and $v_3$ vs multiplicity were plotted to check whether L+R binning on top of centrality binning (by multiplicity) follow the centrality binning trend. The white open circles in all the following plots denote the centrality averaged values (wherever they appear) whereas the points of particular colour and shape (as given in legend) denote the averaged values for different L+R bins within each

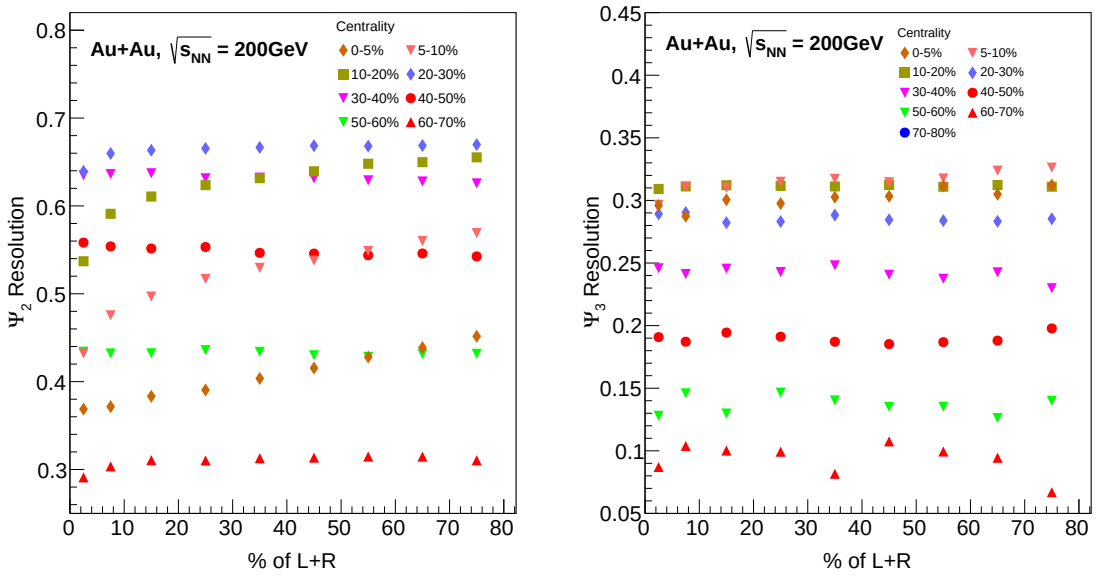


Figure 8.16: Left: $\psi_2$ Resolution, Right: $\psi_3$ Resolutions variations in L+R bins from each centrality.

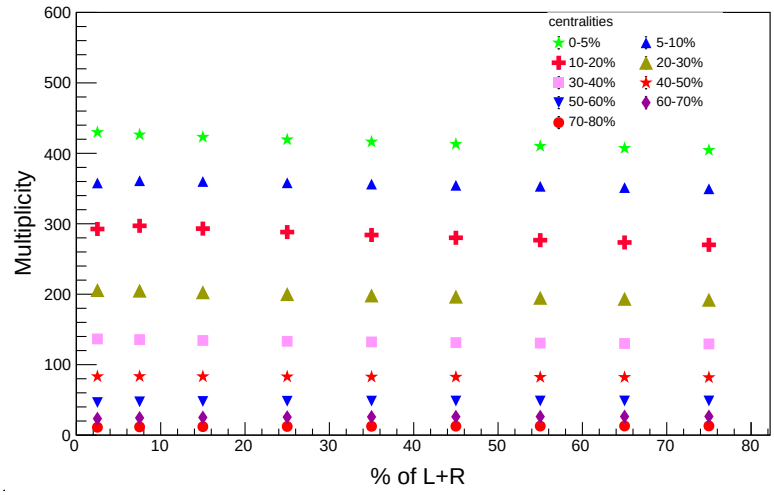


Figure 8.17: Variation of multiplicity for spectator binning in each centrality.

centrality (by multiplicity).

As can be observed from Fig. 8.18, the $v_2$ peaks at intermediate value of centrality in agreement to the fact that the $v_2$ is proportional to the product of $\epsilon_2$ and particle number density. In the most central event, particle density is high but eccentricity

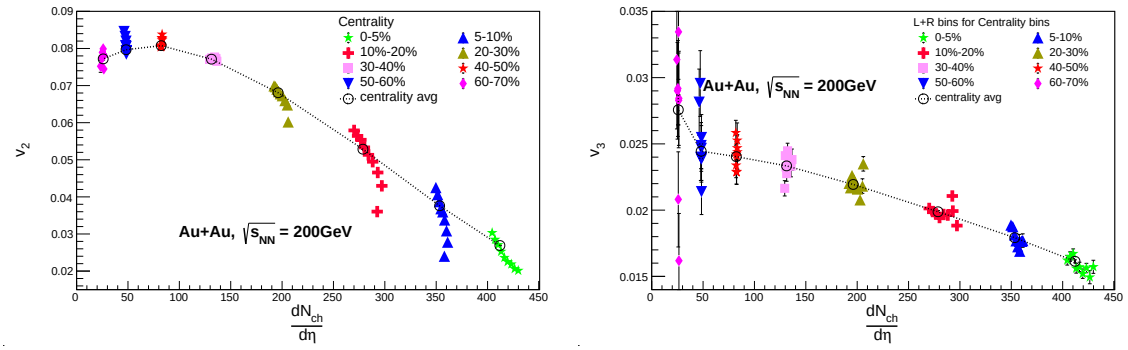


Figure 8.18: Left: $v_2$ vs multiplicity, Right: $v_3$ vs multiplicity, for different centralities and L+R binning on top of centrality bins.

is low and vice-versa for peripheral collisions. The centrality average only reflects an averaged-out effect of all the L+R bins in all the centrality bins. The L+R binning breaks the trend followed by centrality averaged values.

Fig. 8.18 also allows us to conclude that including the L+R binning on top of the centrality binning allows us to more selectively choose events with particular Initial conditions.

Alongwith similar conclusion for $v_3$ vs multiplicity, the variation of dependency from $v_2$ vs multiplicity points towards a change in nature of distribution of flow coefficients for different 'n' in each centrality.

The $v_n$ is proportional to initial overlapping region elliptic-anisotropy, $\epsilon$ and $\frac{1}{S}\frac{dN_{ch}}{d\eta}$ for low particle density, i.e

$$\frac{v_2}{\epsilon_2} \propto \frac{1}{S}\frac{dN_{ch}}{dy}$$

where $S = \pi R_x.R_y$ is the overlapping region area.

To extract overlap region area alongwith other experimental initial conditions (eg: eccentricity, $N_{part}$, $N_{part}$ etc.) Glauber MC model was used. $10^5$ events were generated and analysed. Just like the L+R distribution for each centrality was further subdivided in data obtained from STAR experiment, the spectator nucleon distribu-

tion in each centrality obtained from Glauber MC model was also sub-divided (Fig. 8.19):

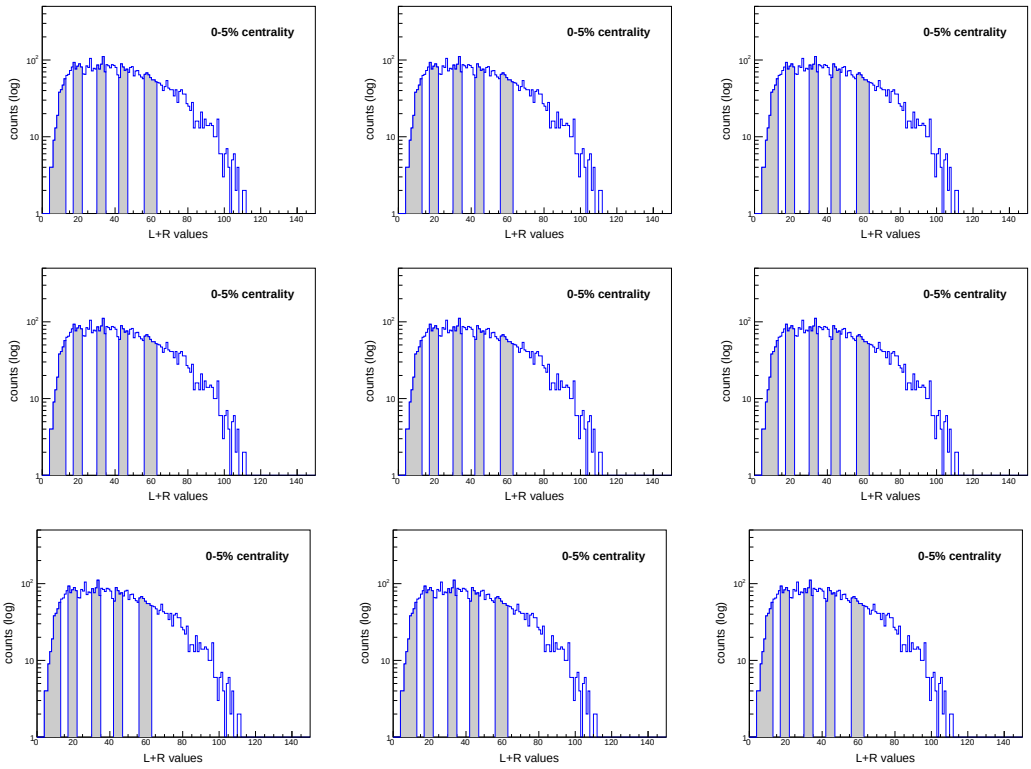


Figure 8.19: Spectator distribution for each centrality (by multiplicity) from Glauber model subdivided into bins of 0-5%,5-10%,10-20%,....70-80% and 80-100%.

Following the sub-division of L+R distribution in each centrality, the experimental observables were extracted from each L+R sub-bin from Glauber model and was implemented in the subsequent analysis.

For checking whether the simulated data is correct, results from Glauber MC were compared with published data (Fig. 8.20) [13].

The extracted values for $\sigma$ varies from published data by 2.9% within error limits whereas the $\epsilon_2$ values varies from published data by 3.2% within error limits (Fig. 8.20).

To validate the Glauber model calculations, the multiplicity obtained from data

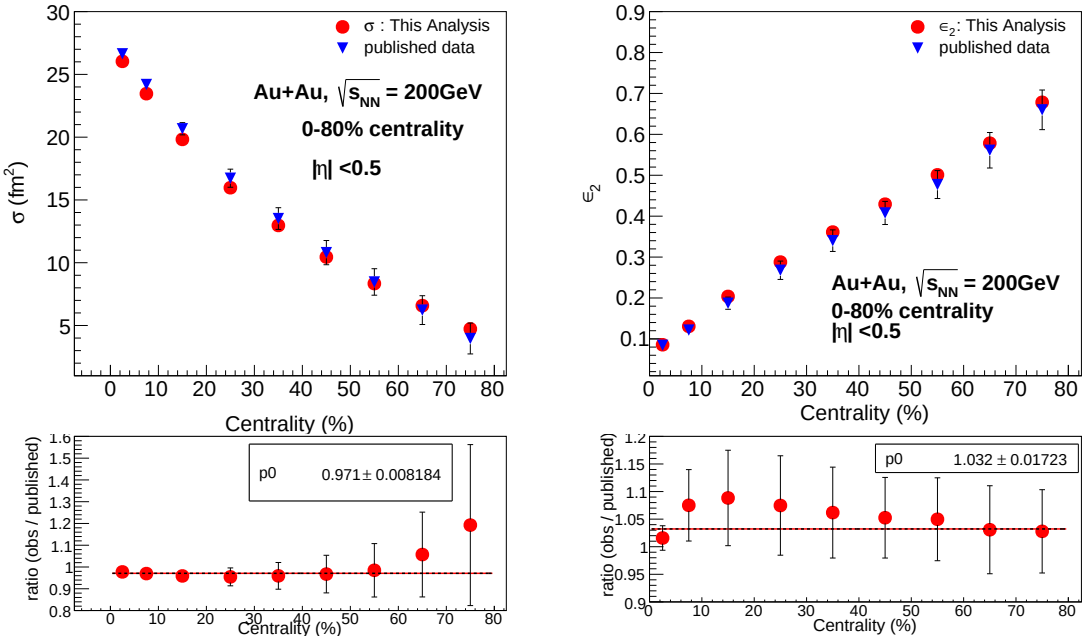


Figure 8.20: Left: Comparison of overlap region area obtained from data and glauber model [13], Right: Comparison of $\epsilon_2$ obtained from data and glauber model [13].

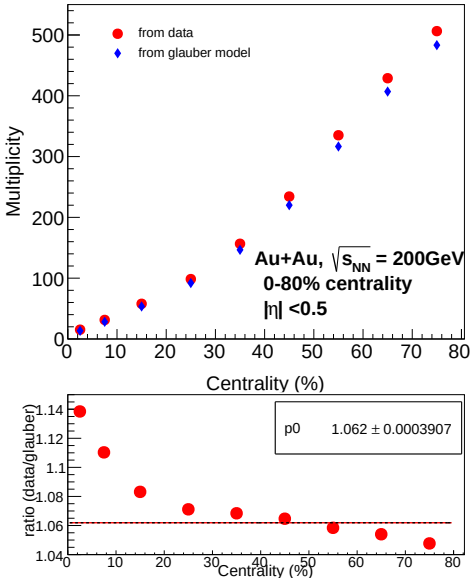


Figure 8.21: Comparison of multiplicity obtained from data and glauber model.

and the multiplicity obtained from Glauber model were compared in each centrality (Fig. 8.21). The extracted values for multiplicity from Glauber model varies from the multiplicity (uncorrected for efficiency) collected from STAR experiment by 6.2% within error limits (Fig. 8.21).

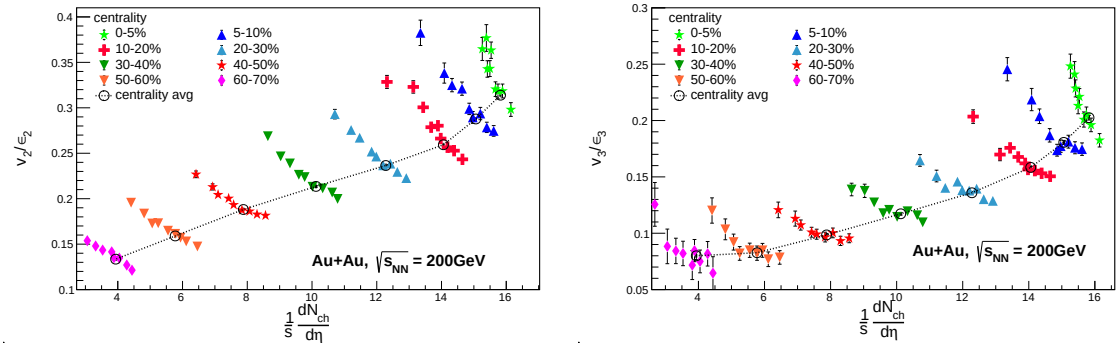


Figure 8.22: Left: $< v_2 > / < \epsilon_2 >$ vs scaled multiplicity, Right: $< v_3 > / < \epsilon_3 >$ vs scaled multiplicity for different centralities and L+R binning on top of centrality bins.

Previous analysis of experimental data with centrality binning have indeed found very good scaling relation between $\frac{\langle v_2 \rangle}{\langle \epsilon_2 \rangle}$ vs $\frac{1}{s}\frac{dN_{ch}}{d\eta}$ for different systems like Cu+Cu and Au+Au [18]. $\frac{\langle v_2 \rangle}{\langle \epsilon_2 \rangle}$ increases with $\frac{1}{s}\frac{dN_{ch}}{dy}$ in centrality binning (Fig. 8.22). This figure shows that although the scaling relation is obeyed by the centrality binning, it is strongly broken in the spectator bins. We observe similar trend for $\frac{\langle v_3 \rangle}{\langle \epsilon_3 \rangle}$ vs $\frac{1}{S}\frac{dN_{ch}}{dy}$.

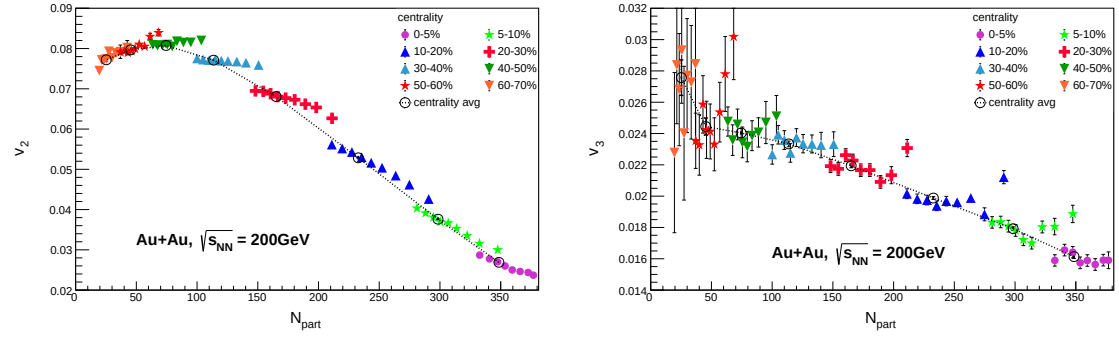


Figure 8.23: Left: $v_2$ vs $N_{part}$, Right: $v_3$ vs $N_{part}$ for different centralities and subsequent L+R binning in each centrality.

In Fig. 8.23, $v_2$ and $v_3$ are plotted vs $N_{part}$. For centrality averaged values, as we move from central to peripheral events, $v_2$ increases with decrease in $N_{part}$ until mid-centralities where the effect of decreasing number of particle sets in. But, the spectator bins break this dependence. With same $N_{part}$, events with different $v_2$ can be chosen using spectator binning (Fig. 8.23).

The $v_3$ varies more closely in each centrality compared to $v_2$ with $N_{part}$. With same $N_{part}$, we can also choose events with different $v_3$ using spectator binning (Fig. 8.23).

As impact parameter decreases the number of participating nucleons is expected to increase.

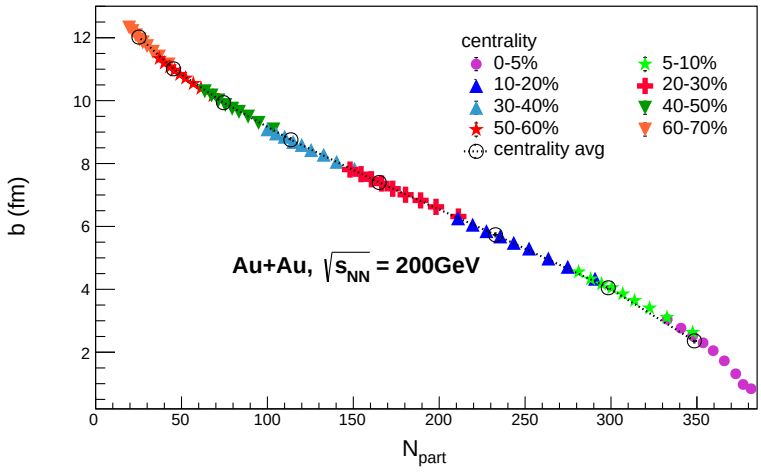


Figure 8.24: The dependence of impact parameter (b) on number of participating nucleons ($N_{part}$).

In Fig. 8.24 we have impact parameter vs number of participating nucleons. We observe that the centrality trend perfectly matches with the subsequent L+R binning values for each centrality.

For eccentricity vs $N_{coll}$ plot(Fig. 8.25), as we move from central to peripheral collisions, the eccentricity of the overlap region increases and the number of binary

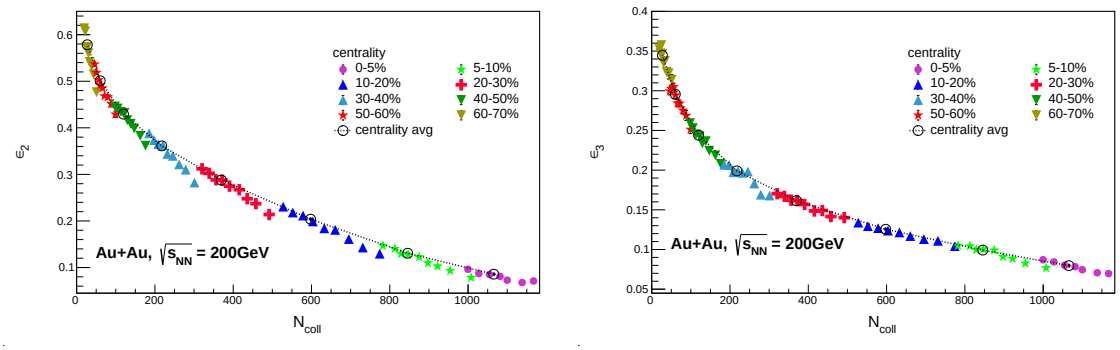


Figure 8.25: Left: $\epsilon_2$ vs $N_{coll}$, Right: $\epsilon_3$ vs $N_{coll}$ for centrality bins and Subsequent L+R bins for each centrality.

collisions decreases. The centrality dependence for eccentricity vs $N_{coll}$ is slightly broken by the spectator binning in each centrality.

For $\epsilon_3$, the variation in each centrality is tighter compared to $\epsilon_2$ vs $N_{coll}$. But still there is a slight deviation from centrality trend.

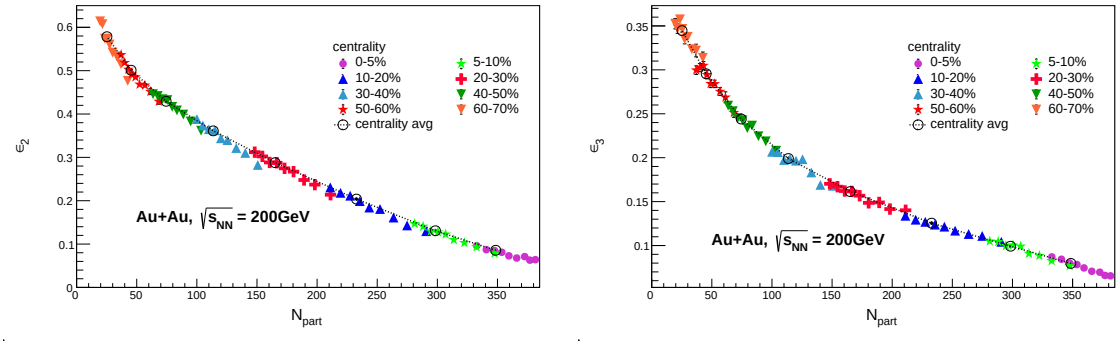


Figure 8.26: Left: $\epsilon_2$ vs $N_{part}$, Right: $\epsilon_3$ vs $N_{part}$ for centrality bins and Subsequent L+R bins for each centrality.

For eccentricity vs $N_{part}$ (Fig. 8.26), there is a slight deviation in trend followed by L+R bins when compared with the centrality binning trend. For $\epsilon_3$, vs $N_{part}$ there is lighter centrality trend breaking when compared with the extent of centrality trend breaking in $\epsilon_2$ vs $N_{part}$.

For eccentricity vs charged particle multiplicity, as the eccentricity decreases, mul-

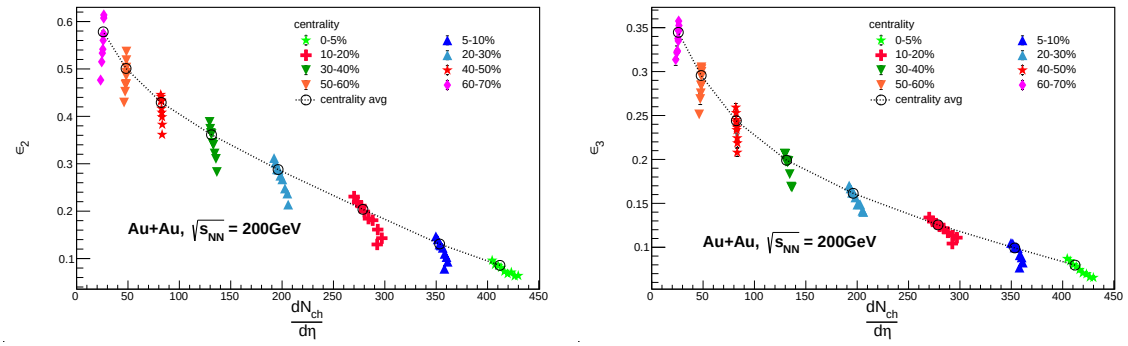


Figure 8.27: Left: $\epsilon_2$ vs Charged particle multiplicity, Right: $\epsilon_3$ vs Charged particle multiplicity for different centralities and subsequent L+R bins in each centrality.

tiplicity increases in centrality binning as expected (Fig. 8.27). The centrality trend is strongly broken by the spectator binning, the degree of centrality trend breaking decreasing as we move from peripheral to central collisions. Using spectator binning we can select events with same eccentricity but a wider range of multiplicity. The events which lie outside the line joining the centrality averages, cannot be accessed even by finer centrality definition. This strengthens the position for this new binning procedure in the direction of studying heavy ion collisions in depth.

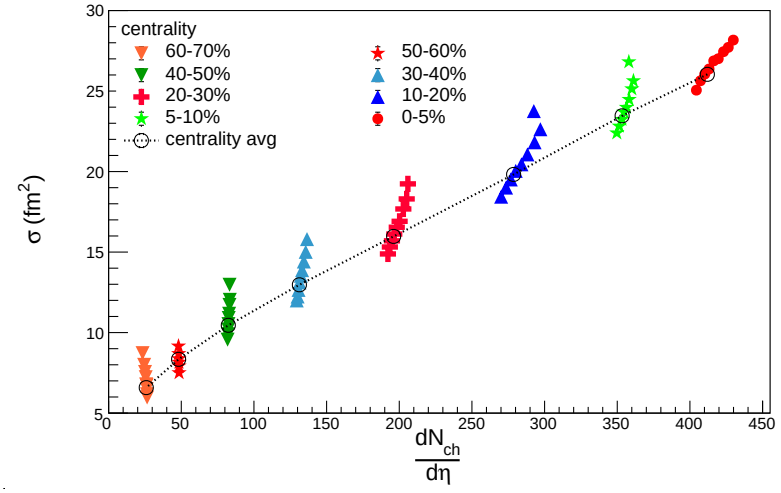


Figure 8.28: Overlap region area vs charged particle multiplicity.

In centrality binning as the overlap region size increases, multiplicity increases as

expected (Fig. 8.28). The centrality trend is strongly broken by the spectator binning, the strength of centrality trend breaking being different for different centralities. We can obtain events with same overlap region but different multiplicities using spectator binning. The L+R binning thus gives us an access to those events whose overlap region area were not accessible as they do not fall on the centrality averaged trend.

Similarly, if we observe the distribution for $\sigma_x$ and $\sigma_y$ vs $N_{part}$ (Fig. 8.29), we observe that in centrality binning, as the $N_{part}$ increases, overlap region size along x and y both increase as expected.

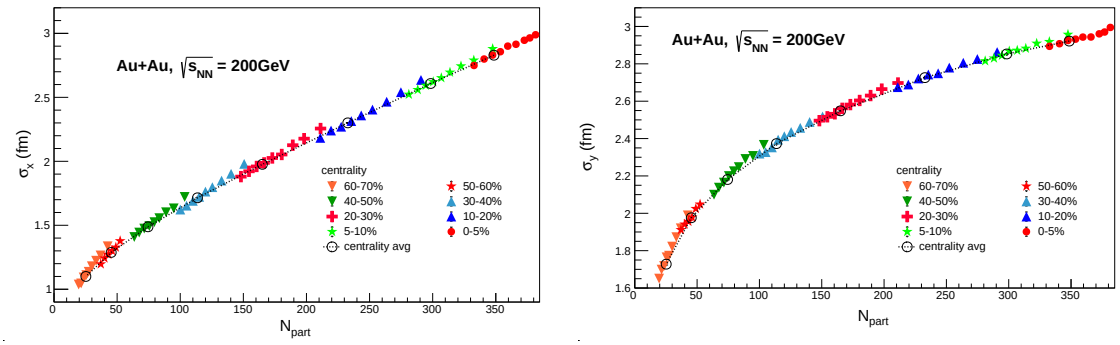


Figure 8.29: Left: $\sigma_x$ vs $N_{part}$ Right: $\sigma_y$ vs $N_{part}$, for centrality binning and subsequent L+R binning for each centrality.

L+R binning mildly breaks the centrality trend for $\sigma_x$ and $\sigma_y$ vs $N_{part}$. The overlap region area spread along y is more than the spread along x.

For charged particle multiplicity vs $N_{coll}$, charged particle multiplicity increases with increasing number of participating nucleons in centrality binning (Fig. 8.30). The centrality trend is strongly broken by the spectator binning. By applying L+R binning on top of conventional centrality (based on charged particle multiplicity) binning, we can access those events which cannot be accessed even by finer centrality definitions. Fig. 8.30 also shows that multiplicity is also guided by factors other than participating nucleons.

Another way of observing the same effect in greater detail is to plot the $\frac{dN_{ch}}{d\eta}/N_{part}$

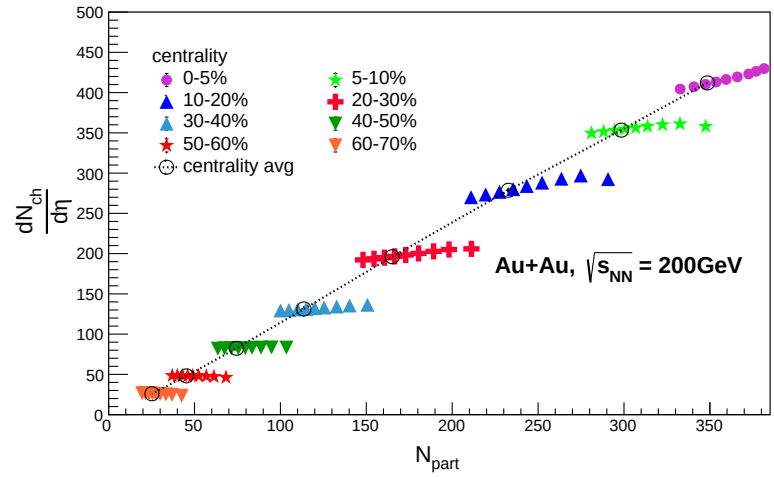


Figure 8.30: Multiplicity vs $N_{part}$.

vs $N_{part}$ as shown in Fig. 8.31:

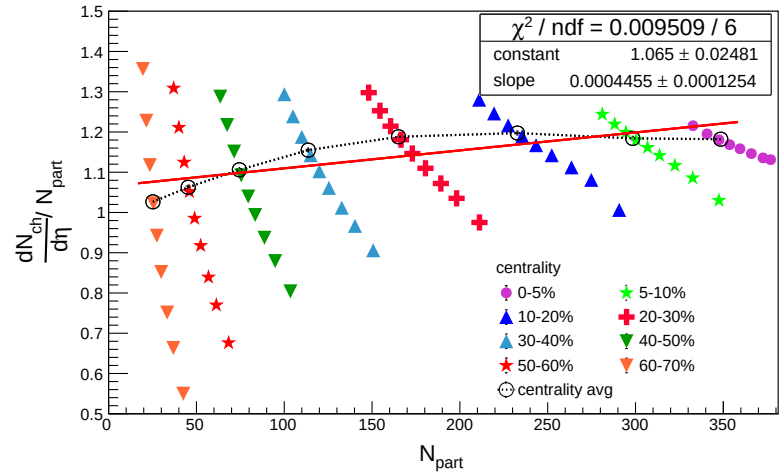


Figure 8.31: Multiplicity scaled by number of participating nucleons($N_{part}$) vs $N_{part}$.

In centrality binning, multiplicity seems to be linearly dependent upon $N_{part}$. But this linearity is strongly broken in the spectator bins, the degree of centrality trend breaking increasing with decreasing centrality (Fig. 8.31).

It is propsed that $N_{coll}$ varies as $N_{part}^{4/3}$ [19]. For a check, we plot $N_{coll}$ vs $N_{part}$ and observe that the proportionality is obeyed in both Centrality binning and spectator

binning (Fig. 8.32). But when the $N_{coll}$ is scaled by $N_{part}^{4/3}$, the plot is expected to be a constant in both centrality and L+R binning. In contrast, although the centrality averages almost falls on a constant line (within error bars), the L+R binning strongly breaks this trend.

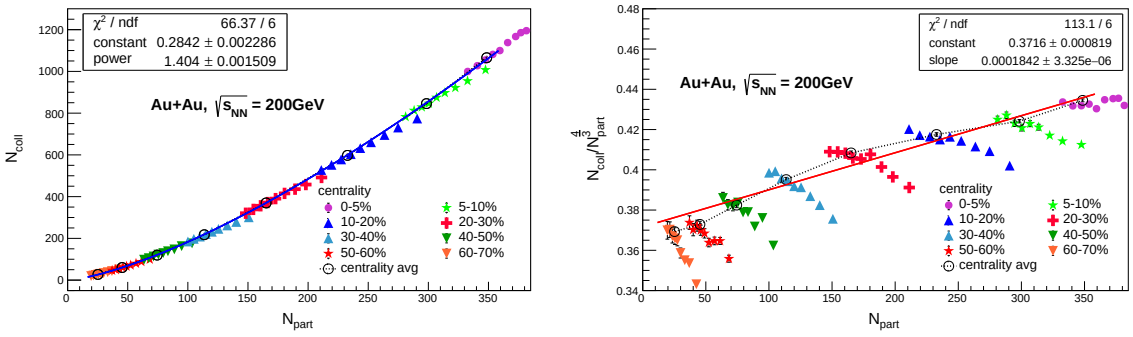


Figure 8.32: Left: $N_{coll}$ vs $N_{part}$, Right: $N_{coll}/N_{part}^{4/3}$ vs $N_{part}$.

The number of binary collisions is expected to increase with increase in the number of participating nucleons.

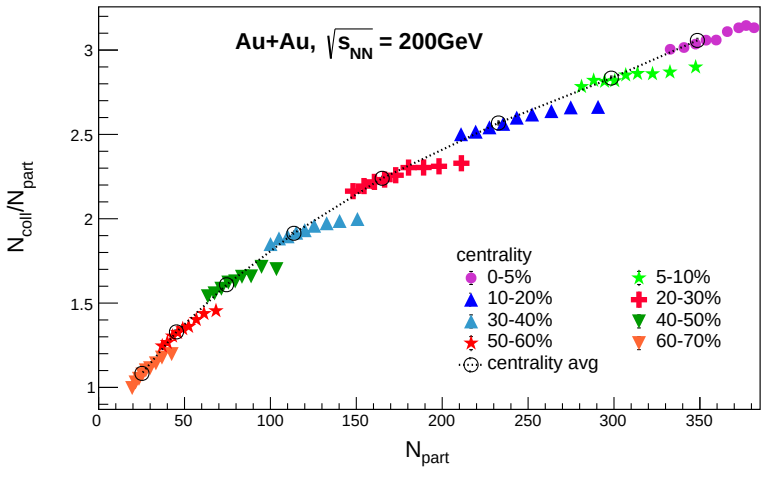


Figure 8.33: $N_{coll}/N_{part}$ vs $N_{part}$ for different centralities and subsequent L+R bins.

It can be clearly seen that for $N_{coll}/N_{part}$ vs $N_{part}$, the centrality trend is strongly broken by the spectator binning (Fig. 8.33). Also, the spectator bins for central

collisions have larger value of $N_{coll}$ compared to a mid-central collisions. This is because in bins with same $N_{part}$ but higher centrality, the participant nucleons are accumulated in a smaller area leading to higher $N_{coll}$.

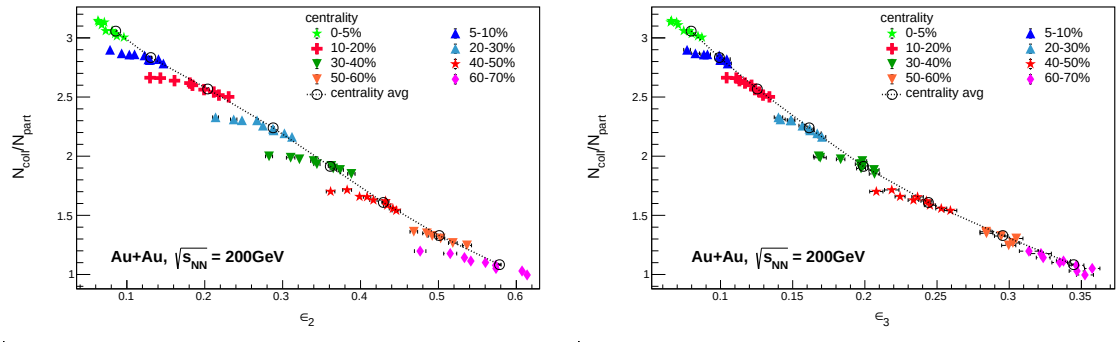


Figure 8.34: Left: $N_{coll}/N_{part}$ vs $\epsilon_2$, Right: $N_{coll}/N_{part}$ vs $\epsilon_3$ in centrality binning and subsequent spectator binning.

In centrality binning, as eccentricity decreases, $N_{coll}/N_{part}$ increases as expected (Fig. 8.34). The spectator binning strongly breaks the centrality trend. The spectator bins for a higher centrality have larger values of $N_{coll}/N_{part}$ compared to a lower centrality. In bins with similar value of $\epsilon_2$ but higher centrality, the participant nucleons are accumulated in a smaller area leading to higher $N_{coll}$. Also, we can select events with similar $N_{coll}/N_{part}$ for a wide range of eccentricity using L+R bins. The centrality trend is also broken by the L+R binning for $N_{coll}/N_{part}$ vs $\epsilon_3$.

Elliptic flow is proportional to the eccentricity of the overlap region and the multiplicity of the event. So we expect the centrality averages of $v_2$ to increase with $\epsilon_2$ until mid centralities before starting to decrease.

As can be seen in centrality bins, $v_2$ increases with $\epsilon_2$ until mid-centralities (Fig. 8.35). But, the spectator bins strongly break this dependence. Using spectator binning we can select events with same $\epsilon_2$ but different $v_2$. We can also select events with specific ($v_2$,$\epsilon_2$) which cant be accessed by finer centrality definition.

As $v_3$ comes from fluctuations in each centrality its magnitude does not vary as

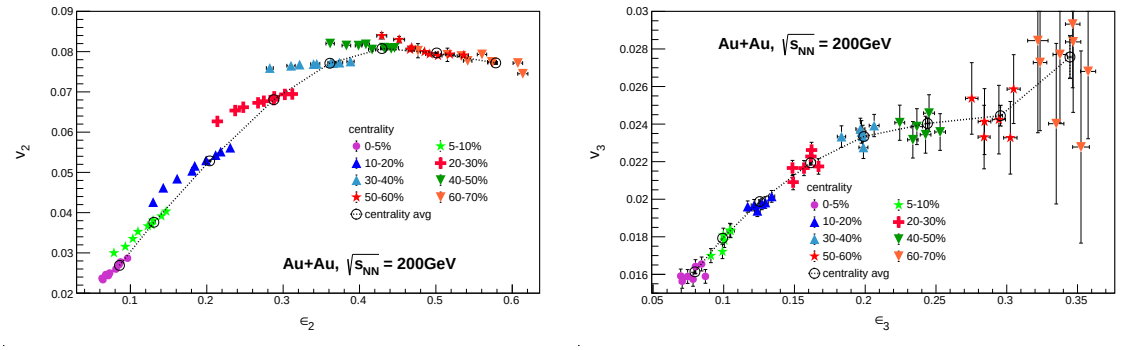


Figure 8.35: Left: $v_2$ vs $\epsilon_2$, Right: $v_3$ vs $\epsilon_3$ for centrality binning and subsequent L+R binning.

much as $v_2$. The $v_3$ vs $\epsilon_3$ values in L+R bins lie closer to centrality trend as compared to those for $v_2$ vs $\epsilon_2$ .

It is proposed that $v_2/\epsilon_2$ shows a scaling relation with $N_{part}^{1/3}$ [20]. In Fig. 8.36, we observe that $v_2/\epsilon_2$ follows the proposed scaling within errors. But, the spectator binning breaks that trend (Fig. 8.36). Moreover the resulting independence of $\frac{v_2/\epsilon_2}{N_{part}^{1/3}}$ on $N_{part}^{1/3}$ is also not followed in the spectator bins for any centrality.

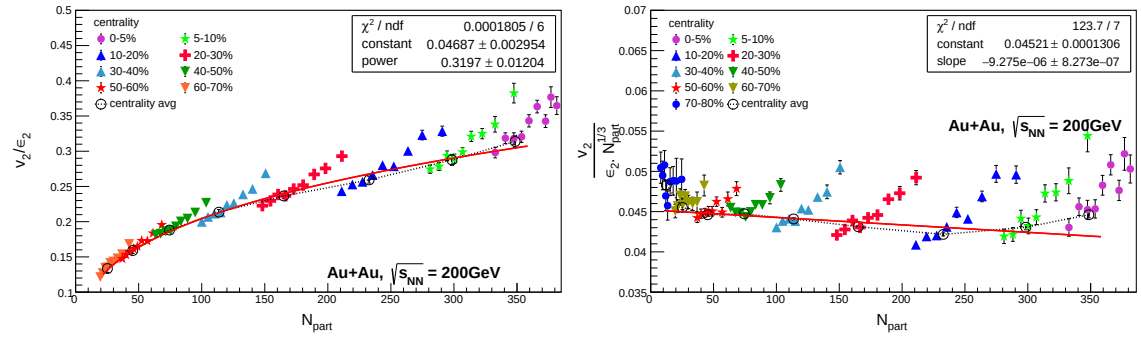


Figure 8.36: Left: $v_2/\epsilon_2$ vs $N_{part}$, Right: $\frac{v_2/\epsilon_2}{N_{part}^{1/3}}$ vs $N_{part}^{1/3}$ for centrality averages and L+R binning for each centrality.

$\frac{v_2/\epsilon_2}{N_{part}^{1/3}}$ vs $N_{part}$ is a proposed scaling to check thermalisation of the system. In case of thermalisation it has no dependency on $N_{part}$ [20]. As can be seen it is almost a constant for centrality binning. But the Spectator binning breaks this linearity (Fig.

8.36).

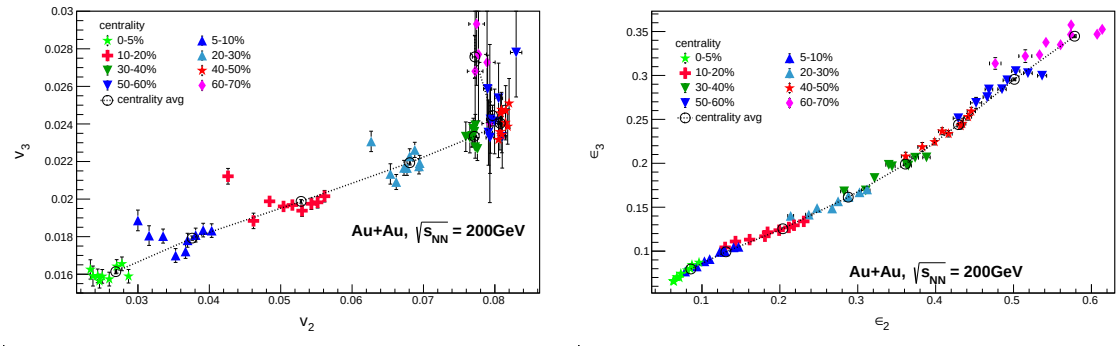


Figure 8.37: Left: $v_2$ vs $v_3$, Right: $\epsilon_2$ vs $\epsilon_3$ for different centralities and subsequent L+R bins.

From the figure for $v_2$ vs $v_3$ (Fig. 8.37), we can observe that many L+R averaged values lie away from the centrality average trend. Thus, L+R binning allows us to select events with a wider range of very specific ($v_2$ ,$v_3$) compared to only centrality binning. These events with highly specific ($v_2$ ,$v_3$) cannot be selected from even the finest of centrality definition (eg. 0-1%, 1-2%, ....79-80%) alone as the points extracted from any fine centrality definition (using multiplicity) will lie on the centrality trend line. From $\epsilon_2$ vs $\epsilon_3$ plot(Fig. 8.37) it can be observed that the L+R binning closely follows the centrality trend.

The ratio $v_n/\epsilon_n$ is also expected to exhibit acoustic scaling [21-22] and receives viscous corrections that grow exponentially as $n^2$ and $1/\Lambda$

$$ln(\frac{v_n}{\epsilon_n}) \sim -\frac{4}{3}\frac{n^2\eta}{\Lambda_T T s}$$

where $\Lambda_T = \sqrt{\frac{1}{\sigma_x^2} + \frac{1}{\sigma_y^2}}$. Such acoustic scaling is found in data across a wide range of beam energies and the shear viscosity to entropy density ratio, $\eta/s$ is extracted from the slope of the plot, $\ln(v_2/\epsilon_2)$ vs $1/\Lambda_T$. These studies were done with centrality binning alone. The Acoustic scaling was checked by plotting $v_2/\epsilon_2$ and $v_3/\epsilon_3$ vs $1/\Lambda_T$

(Fig. 8.38) for each entrality and each L+R bin within all centralities.

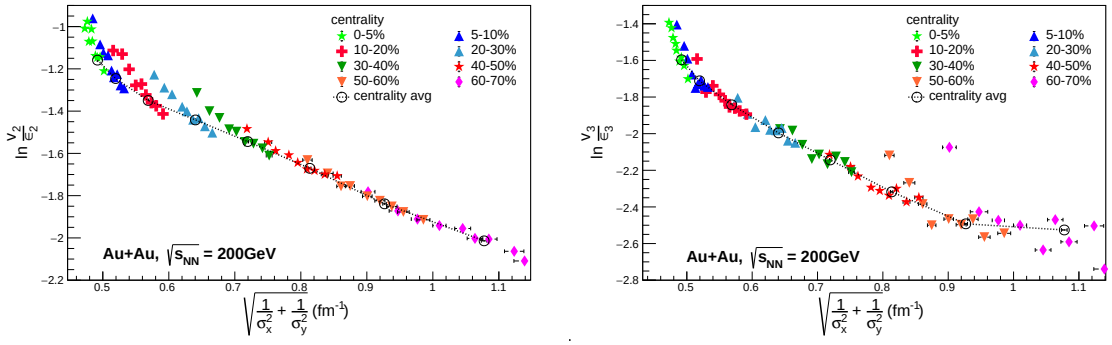


Figure 8.38: Left: $v_2/\epsilon_2$ vs $1/\Lambda_T$, Right: $v_3/\epsilon_3$ vs $1/\Lambda_T$ for Different centralities and subsequent L+R bins in each centrality.

The slope for bins of different L + R but a particular centrality is different from those of a different centrality resulting in a mild breaking of the acoustic scaling. Thus, the introduction of the L+R bins can enable a more refined extraction of $\eta/s$ from data.

# Chapter 9

# Conclusion

The centrality binning highly limits our capabilities at accessing the variation of characteristics of events in heavy ion collision. It can be concluded from the observations in this work that these variations of events in each centralities can be accessed by this new procedure of categorization of events. The L+R binning on top of centrality binning allows us to access those events which could not be accessed even by finer centrality definitions. Moreover, this novel binning procedure also allows us to study some previously postulated scaling relations for centrality averaged values such as $(\frac{v_n}{\epsilon_n})$ vs $\frac{1}{S}\frac{dN_{ch}}{d\eta}$ and acoustic scaling relations in greater details.

# Chapter 10

# Future Plan

We are currently trying to obtain and use the efficiency corrected charged particle multiplicity. Moreover, the ZDC distribution used in this work corresponds to the ADC counts coming from the ZDC in both directions whereas the spectator number distribution obtained from Glauber model consists of total number of neutrons and protons. Although the binning is done in a way to take corresponding events from data and Glauber MC model for analysis, we need to develop a formulation to obtain the spectator number distribution from ZDC data too for a better comparison. These will surely add to the robustness of the new binning procedure. Also, we wish to study in future if the reverse order of binning in data affects our conclusions.

# Bibliography


1. Vipul Bairathi et al., *Phys. Lett. B* **754**, 144-150 (2016).
2. S. L. Glashow, *Nucl. Phys.* **22**, 579 (1961). A. Salam and J.C. Ward, *Phys. Lett.*, **168** 168 (1964).
3. N.V.D Kolk thesis, Utrecht University (2011), link.
4. Coupling Constants for the Fundamental Forces, link.
5. H. Fritzsch, *Phys.Usp.* **52**, 359-367 (2009).
6. Rihan Haque's thesis, National Institute of Science Education and Research (2015), link.
7. Popular Information from Nobel Prize Org., link.
8. Gines Martinez, *arXiv:1304:1452v1 [nucl-ex].* (2013).
9. Deuteron-gold collisions clarify 'jet quenching' results, link.
10. J. Adams et al., *Phys.Rev.C* **72**, 014904 (2005).
11. K.H. Ackermann et al., *Nucl.Instrum.Meth. A* **499**, 624-632 (2003).
12. Voloshin, Poskanzer, Phys.Lett. B **474**, 27-32 (2000).
13. H. Masui et.al, *Phys.Lett.B* **679**, 440-444 (2009).
14. ROOT users guide, (https://root.cern.ch/guides/users-guide).
15. L Adamczyk et.al., *Phys Rev C.* **94**, 034908 (2016).
16. Jean-Yves Ollitrault, *Eur.J.Phys.* **29**, 275-302 (2008).
17. B.I. Abelev et al, *Phys.Rev.C* **77**, 054901 (2008).
18. Huichao Song et. al, *Phys. Rev. Lett.* **106**, 192301 (2011).
19. Miller et.al., *Ann.Rev.Nucl.Part.Sci.* **57**, 205-243 (2007).
20. Maya Shimomura et.al, *Nucl.Phys.A* **830**, 183c-186c (2009).
21. R. A. Lacey, A. Taranenko et. al., *arXiv:1105.3782 [nucl-ex]*, (2011).
22. R. A. Lacey et al., *arXiv:1301.0165 [nucl-ex]*, (2018).